Site preferences and jump frequencies of In/Cd solutes in rare earth palladium phases having the L1$_2$ structure

by

Wang, Qiaoming

May 2012

Hyperfine Interactions Group
Department of Physics and Astronomy
Washington State University
Pullman, Washington 99164
USA

Foreword

This report includes the MS thesis of Qiaoming Wang, defended April 26, 2012. An addendum is attached at the end that provides additional information and results based on the research. The research described herein was supported in part by the National Science Foundation under grant DMR 09-04096 (Metals Program).

Gary S. Collins
collins@wsu.edu
July 2012

SITE PREFERENCES AND JUMP FREQUENCIES OF In/Cd

SOLUTES IN RARE EARTH PALLADIUM PHASES

HAVING THE L1$_2$ STRUCTURE

By

WANG, QIAOMING

王　巧鸣

A thesis submitted in partial fulfillment of
the requirement for the degree of

MASTER OF SCIENCE IN PHYSICS

WASHINGTON STATE UNIVERSITY
Department of Physics and Astronomy

MAY 2012

To the Faculty of Washington State University

The members of the Committee appointed to examine the thesis of QIAOMING WANG find it satisfactory and recommend that it be accepted.

Committee:

_____
Gary S. Collins, Chair

_____
Kelvin Lynn

_____
Farida A. Selim

ACKNOWLEDGEMENT

I would like to thank my advisor professor Gary S. Collins for his great assistance in my choice of research topics, for his patient guidance in the analysis of experimental data and response to my questions.

My thanks go to Randal Newhouse for his kind help in sample preparation and data processing, and fixing the instrumental problems.

I would also like to thank Xiangyu Yin, Lee Aspitarte and Jesse Miller for their help and advice on my experiments.

I would like to appreciate my family for their encouragement and support during my study.

SITE PREFERENCES AND JUMP FREQUENCIES OF In/Cd

SOLUTES IN RARE EARTH PALLADIUM PHASES

HAVING THE L1$_2$ STRUCTURE

Abstract

By Qiaoming Wang M.S.
Washington State University
May 2012

Chair: Gary S. Collins

The method of Perturbed Angular Correlation of gamma rays (PAC) was used to study site preferences of indium solutes and jump frequencies of cadmium impurities in rare-earth palladium phases RPd$_3$ which has the L1$_2$ structure (prototype AuCu$_3$), including both Pd-poorer and Pd-richer samples. It was found that indium solutes always occupied rare-earth sites in Pd-richer samples. In Pd-poorer samples, indium preferentially occupied the rare-earth site for light rare-earth palladides (R=La and Ce), both rare-earth site and Pd-site for R=Ce, Pr, Nd, Sm and Eu, and almost entirely occupies the Pd site for R=Tb, Er, Yb and Lu. The sites occupied were resolved through measurements of the nuclear quadrupole interactions at ^{111}In probe nuclei. For R=Ce, Pr, Nd, Sm and Eu, transfer enthalpies between R-sites and Pd-sites were determined through temperature dependences of the site fractions. The enthalpies were found to change sign along the series R=Ce, Pr, Nd, Sm and Eu, with indium solutes having lower enthalpy on rare-earth sites for R=Ce and on Pd-sites for R=Eu.

For the series of rare-earth palladides, quadrupole interaction frequencies of cadmium impurities on Pd-sublattice were found to be ~ 110Mrad/s for intermediate and heavy rare-earth palladides. Surprisingly, the frequencies were observed to *decrease* along the series from R=Pr to Lu, in spite of a decrease on the lattice parameter. In addition, temperature dependences of the quadrupole interaction frequencies were found to be much greater for R=Pr than for R=Lu.

Quadrupole interaction frequencies of different L1$_2$ phases were compared using a point charge model.

Jump frequencies of cadmium impurities on the Pd-sublattice were determined from fits of nuclear relaxation for R=Ce, Pr, Nd, Sm and Eu, and activation enthalpies were extracted from the Arrhenius temperature dependence of their jump frequencies. Activation enthalpies increases from 0.20 eV for R=Ce to 2.19 eV for R=Sm. Jump frequencies of rare-earth palladides were compared with those observed in indides, gallides, aluminides, stannides and plumbides having the L1$_2$ structure, and found to be generally the largest.

TABLE OF CONTENTS

LIST OF TABLES

LIST OF FIGURES

Chapter 1: Introduction

Site occupation changes or site preference of solutes in intermetallic compounds has long been an interesting field in nuclear condensed matter physics. Many experiments have been explored to investigate the site preferences, including Mossbauer experiments by P. Chartier et al. [1], the atom location channeling enhanced microanalysis (ALCHEMI) method by Y. L. Hao et al. [2], and the Perturbed Angular Correlation (PAC) of gamma rays experiments by M. O. Zacate et al. [3].

In this thesis changes of site occupation of indium solutes in rare-earth palladium phases RPd_3 were studied using PAC experiments. In PAC technique, nuclear states of probe atom under magnetic field or electric field gradient (EFG) can be studied and the locations of solutes are determined by quadrupole interaction frequencies in the spectra. Changes of site occupation are therefore characterized by the variation of the site-fraction of each signal. The present work focuses on the binary intermetallic phases RPd_3 having the $L1_2$ structure A_3B (prototype: $AuCu_3$), which is a face-center-cubic based structure (see Fig. 1). In the phase RPd_3, R atoms are in the corners of the conventional unit cell and Pd atoms occupy the face centers. Each R atom has 12 Pd nearest neighbors, while each Pd atom is surrounded by 8 R atom and 4 Pd atom as nearest neighbors. Note that almost all RPd_3 phases have phase widths ranging from maximum Pd-composition to minimum Pd-composition, different from "line" compounds (definite composition, such as A:B=75:25).

Diffusion in solids is another topic which causes great interest in condensed matter physics. In PAC experiments, diffusion in intermetallic compounds is characterized by jumping of nuclear solutes, which are cadmium nuclei in the present work when ^{111}In source is used. Specifically, jumping of cadmium solutes causes reorientation of EFG directions and leads to dynamical relaxation and damping of the perturbation function. Jump frequency of cadmium tracer in In_3La was studied by M. O. Zacate et al. [4] and dependence of the diffusion mechanism on lattice constant in In_3R was considered by G. S. Collins et al. [5]. In the present work, jump frequencies of cadmium tracer atoms in RPd_3 having the $L1_2$ structure were also studied by PAC technique and compared with other $L1_2$ phases' results (section 5.5). Jump frequencies in the Six series of $L1_2$ phases were summarized and compared, including RIn_3, RPd_3, RGa_3, RAl_3, RSn_3 and RPb_3. As an incidental result, quadrupole interaction frequencies of cadmium impurities for these six

phases were also measured and illustrated by a point charge model (section 5.3 and 5.4).
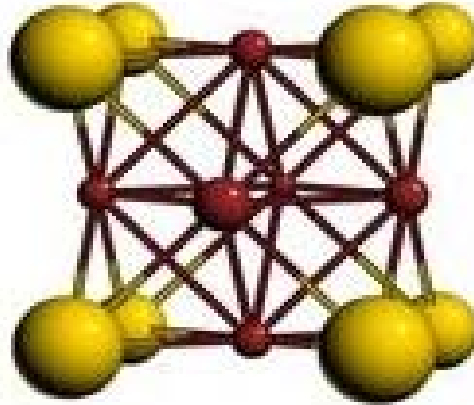
Figure 1. Crystal structure of L1$_2$ Phase. Large yellow sites are rare-earth atoms and small brown ones are Pd atoms.

Chapter 2: EXPERIMENTAL METHODS

2.1 Theories of Perturbed Angular Correlation of Gamma Rays (PAC)

2.1.1 Introduction to PAC

The Perturbed Angular Correlation (PAC) experiments, which was started in the 1940s, [6, 7], use scintillation detectors to collect gamma-gamma cascade to study hyperfine interaction of nuclear states in solids under magnetic field or electric field gradient. Early PAC experiments had already been able to introduce a nuclear probe into the sample, to determine its nuclear spins and parities, or study its hyperfine interaction fields in ferromagnetic materials or chemical compounds and noncubic metals, and also point defects problems in metals can also be addressed by PAC later. There are two generations of PAC point defect studies: the first generation defect studies uses ion implantation to create the point defects and focus on their properties, while the second generation or the modern generation prefers to trap interstitial atoms close to probe atom by using vacancy clusters and make the study of these interstitial atoms possible.

2.1.2 Electric Quadrupole Interaction

The interaction of a nucleus with an electric field or magnetic field is called a hyperfine interaction. The PAC experiments aim to study the hyperfine interaction of probe atoms in electric or magnetic environment. In the case of electric interaction, the energy of a nuclear charge distribution $\rho(r)$ in an external potential $\phi(r)$ is (The equations in Chapter 2 are following closely to Ref. [8] and [9].)

$$E_{electr} = \int \rho(r)\phi(r)d^3r \tag{1}$$

where

$$\int \rho(r)d^3r = Ze \tag{2}$$

the energy can be expanded in a Taylor series around r=0:

$$E_{electr} = E^{(0)} + E^{(1)} + E^{(2)} + \cdots \tag{3}$$

where

$$E^{(0)} = \phi_0 \int \rho(r)d^3r \tag{4}$$

$$E^{(1)} = \sum_{\alpha=1}^{3}(\frac{\partial \phi}{\partial x_\alpha})_0 \int \rho(r)d^3r \tag{5}$$

$$E^{(2)} = \frac{1}{2}\sum_{\alpha,\beta}^{3}(\frac{\partial^2 \phi}{\partial x_\alpha \partial x_\beta})_0 \int \rho(r)x_\alpha x_\beta d^3r \tag{6}$$

The first term $E^{(0)}$ is the Coulomb energy of a point like charge distribution in the external electric potential; the second term $E^{(1)}$ represents an electric dipole interaction of the dipole moment of the charge distribution with the electric field $E = -\nabla\emptyset$ at the origin (r=0); the third term $E^{(2)}$ is the electric quadruple interaction, the quantities

$$(\frac{\partial^2 \phi}{\partial x_\alpha \partial x_\beta})_0 = \phi_{\alpha\beta}$$

can be diagonalized by a coordination and therefore

$$E^{(2)} = \frac{1}{2}\sum_{\alpha} \phi_{\alpha\alpha} \int \rho(r){x_\alpha}^2 d^3r$$

$$= \frac{1}{6}\sum_{\alpha} \phi_{\alpha\alpha} \int \rho(r)r^2 d^3r + \frac{1}{2}\sum_{\alpha} \phi_{\alpha\alpha} \int \rho(r)(x_\alpha^2 - \frac{r^2}{3})d^3r$$

$$E^{(2)} = E_C + E_Q \tag{7}$$

E_C is the monopole term, responsible for the isotope shift in atomic physics. E_Q is the electric quadrupole interaction term, and can be rewritten as

$$E_Q = \frac{e}{6}\sum_{\alpha} \phi_{\alpha\alpha} Q_{\alpha\alpha}$$

where

$$Q_{\alpha\alpha} = \frac{1}{e}\int \rho(r)(3x_\alpha^2 - r^2)d^3r \tag{8}$$

If one defines

$$Q_{\alpha\alpha} = V_{\alpha\alpha} + \frac{1}{3}(\Delta\phi)$$

the portion $\frac{1}{3}(\Delta\phi)$ does not contribute to E_Q since $Q_{\alpha\alpha}$ and $V_{\alpha\alpha}$ are traceless tensors. Thus

E_Q becomes

$$E_Q = \frac{e}{6} \sum_\alpha V_{\alpha\alpha} Q_{\alpha\alpha}$$

$V_{\alpha\alpha}$ is called the electric field gradient (EFG), which has only two independent parameters because of its traceless properties. Basically the appropriate choice of the principle axis system is

$$V_{zz} > V_{yy} > V_{xx}$$

by defining the asymmetry parameter η

$$\eta = \frac{V_{xx} - V_{yy}}{V_{zz}} \tag{9}$$

the EFG can be completely described by V_{zz} and η.

Whereas magnetic fields are common to us through the variety of magnetic materials, this is not the case for electric field gradients. At the site of the nucleus the measured magnetic or electric fields can be modified by various sources, which can fairly well be calculated in the case of magnetic fields, while for electric field gradients in metals appropriate theories are still lacking. Therefore, using PAC in metals can shed light on a better understanding on this problem.

2.1.3 $\gamma - \gamma$ Angular Correlation

The perturbed $\gamma - \gamma$ angular correlation method (PAC) basically study the time dependence of the $\gamma - ray$ emission pattern, which requires γ-rays emitted anisotropically from the probe atoms. Fig. 2 is a scheme of $\gamma - \gamma$ emission illustration. The initial state $|I_i, M_i\rangle$ decays into intermediate state $|I, M\rangle$ by emission of γ_1 and then followed by emission of γ_2 into final state $|I_f, M_f\rangle$. This is an unperturbed angular correlation where M state does not have life time and thus could not be affected by external magnetic field or EFG. The transition amplitudes for the γ-ray emission from $|I_i, M_i\rangle$ to $|I, M\rangle$ and from $|I, M\rangle$ to $|I_f, M_f\rangle$ are

$$\langle I, M, k_1, \sigma_1 | \mathcal{H}_1 | I_i, M_i \rangle \text{ and } \langle I_f, M_f, k_2, \sigma_2 | \mathcal{H}_2 | I, M \rangle$$

where k_1, σ_1 and k_2, σ_2 are the wave vector and polarization of γ_1 and γ_2, respectively. $\mathcal{H}_1$ and $\mathcal{H}_2$ are the interaction Hamiltonian operators for the emission of γ_1 and $\gamma_{2,}$.

The angular correlation is

$$W(M_i \rightarrow M_f) = \left| \sum_M \langle M_f | \mathcal{H}_2 | M \rangle \langle M | \mathcal{H}_1 | M_i \rangle \right|$$

after summing the transition probabilities and calculating the matrix elements [4], the angular correlation is given by

$$W(k_1, k_2) = W(\theta) = \sum_{\substack{k \text{ even}}}^{k_{max}} A_k(1) A_k(2) P_k(\cos\theta)$$

The coefficient $A_k(1)$ depends only on the first transition and $A_k(2)$ depends only on the second.

In perturbed $\gamma - \gamma$ angular correlations the intermediate state $|I, M\rangle$ has a lifetime τ_N and a given initial substate $|M_a\rangle$ in this level will evolve into $|M_b\rangle = \Lambda(t)|M_a\rangle$ during this lifetime, where $\Lambda(t)$ is the time-evolution operator. The perturbed $\gamma - \gamma$ angular correlation is therefore

$$W(k_1, k_2, t) = \sum_{k_1, k_2, N_1, N_2} A_k(1) A_k(2) G_{k_1 k_2}^{N_1 N_2}(t) \frac{1}{\sqrt{(2k_1 + 1)(2k_2 + 1)}} Y_{k_1}^{N_1*}(\theta_1, \phi_1) Y_{k_2}^{N_2}(\theta_2, \phi_2)$$

where $G_{k_1 k_2}^{N_1 N_2}(t)$ is the perturbation factor, which depends on the quantum numbers of the intermediate state. In electric quadrupole interaction, the angular correlation depends only on the angle between k1 and k2, and thus $G_{k_1 k_2}^{N_1 N_2}(t)$ can have the simple formula [11]:

$$W(\theta, t) = \sum_{\substack{k \text{ even}}}^{k_{max}} A_{kk} G_{kk}(t) P_k(\cos\theta) \tag{10}$$

where

$$G_{kk}(t) = \sum_{n=0}^{n_{max}} s_{kn} \cos(n\omega_Q^0 t) \tag{11}$$

Here

$\omega_Q^0 = 3\omega_Q$ for I integral

$\omega_Q^0 = 6\omega_Q$ for I half-integral
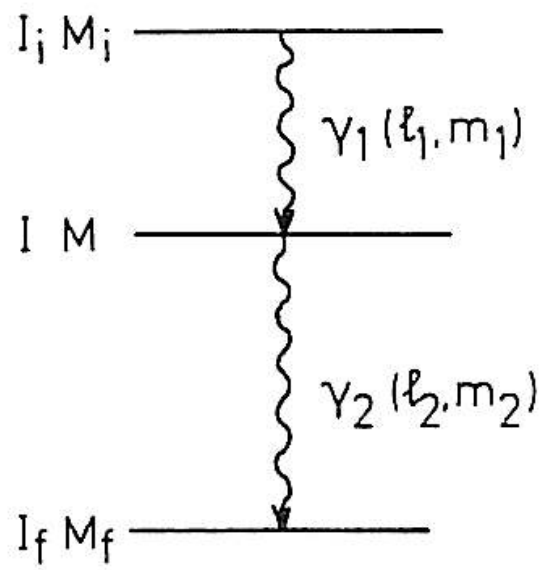
Fig. 2. Illustration of γ-ray emission pattern

2.1.4 Quadrupole Interaction Frequency

In the tensor representation, the electric quadrupole interaction energy is given by [12]:

$$E_Q = \frac{3M^2 - I(I+1)}{4I(2I-1)} eQV_{zz} \tag{12}$$

The transition energy between two sublevels M' and M'' in the intermediate state M is

$$E_Q(M') - E_Q(M'') = \frac{3eQV_{zz}}{4I(2I-1)} |M'^2 - M''^2| = 3|M'^2 - M''^2|\hbar\omega_Q \tag{13}$$

where the fundamental quadrupole frequency is defined as

$$\omega_Q = \frac{eQV_{zz}}{4I(2I-1)\hbar} \tag{14}$$

In the case of ^{111}In probe atoms, the nuclear spin is 5/2, and the energy splitting is shown in Fig. 3.

$$\omega_1 = \frac{E_Q\left(\pm\frac{3}{2}\right) - E_Q\left(\pm\frac{1}{2}\right)}{\hbar} = \frac{3eQV_{zz}}{20\hbar} = 6\omega_Q$$

$$\omega_2 = \frac{E_Q\left(\pm\frac{5}{2}\right) - E_Q\left(\pm\frac{3}{2}\right)}{\hbar} = \frac{6eQV_{zz}}{20\hbar} = 12\omega_Q$$

$$\omega_3 = \omega_1 + \omega_2 = 18\omega_Q$$

the transition frequencies $\omega_1 : \omega_2 : \omega_3$ in the case $\eta = 0$ are in the ratio 1:2:3.

2.2 PAC Experimental Apparatus

2.2.1 PAC sources

In PAC technique, the EFG of radioactive probe atoms is measured by counting the gamma-gamma cascade, to characterize a metal in a microscopic scale. The most commonly used PAC sources are ^{111}In, [181]Hf and [100]Pd. In our experiments, the isotope ^{111}In is used as radioactive probe atoms, which is also the most frequently used PAC sources.

Fig. 3 is the decay scheme of [111]In. [111]In decays to [111]Cd by electric capture (EC), which has three energy levels I =7/2, 5/2 and 1/2. The I=5/2 energy level is an intermediate state having lifetime for only $t_{1/2} = 85ns$, which can be split into six sublevels under external magnetic field or EFG, $|I = \frac{5}{2}, M = \pm\frac{5}{2}, \pm\frac{3}{2}, \pm\frac{1}{2}\rangle$.
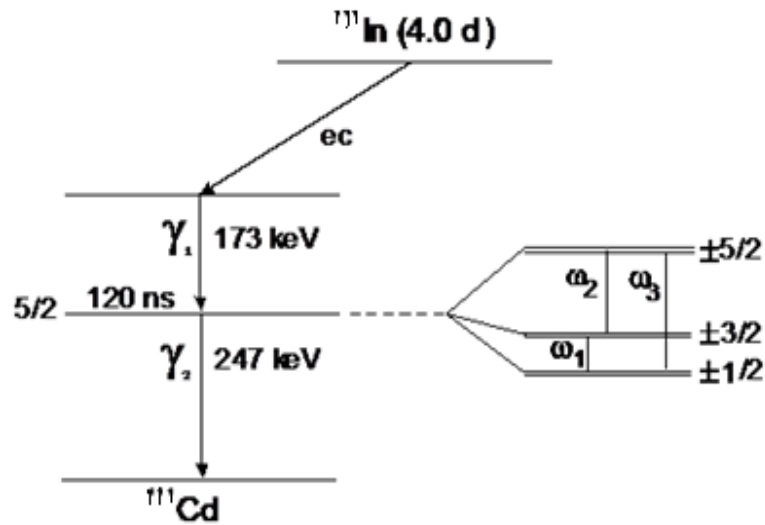
Fig. 3. Decay shecme of [111]In. The right part is the energy splitting of an spin-5/2 level under the influence of an axially symmetric quadrupole interaction.

2.2.2 PAC Experimental Setup

In PAC measurement, four detectors are used to record coincident count rates that oscillate in time with frequencies. The four detectors usually have geometrical scheme shown in Fig. 4, having 90 degree angles with each other. The γ-ray emission pattern sweeps past the detectors

like a lighthouse beam. The first γ-ray (γ_1 in Fig. 3) is used as the start signal, while the second γ-ray (γ_2 in Fig. 3) is used as the stop signal. Every γ-ray is separated into an energy signal and a time signal, which are amplified by a constant fraction discriminator (AMP) (Fig. 5). The energy passes through a single channel to a coincidence circuit, while the time signal is delayed and allowed to pass the coincidence circuit only if the energy has the desired value. The signals are then sent to a time-to-amplitude converter (TAC), where the output is converted to digital values by an analog-to-digital converter (ADC) and stored in a multichannel analyzer.

The coincident count rate N_{ij} between start detector i and stop detector j is [10]

$$N_{ij} = \epsilon_i \epsilon_j \Omega_i \Omega_j N \tag{15}$$

where ϵ_i and ϵ_j are the detector efficiencies, Ω_i and Ω_j are solid angles normalized to 4π, and N is the source activity. If the four detectors are labeled as shown in Fig. 4, the angle θ between detectors $ij = 13, 14, 23, 24$ are π, $\pi/2$, $\pi/2$ and π, respectively. Generally, in PAC experiments, four double-sided spectra need to be collected, which means that each angle θ has two coincident count rate N_{ij}, one in the positive time and the other in the negative time. The perturbation function $G_2(t)$ can be extracted from the number of the differential coincidence count rate at time t for the four detectors

$$C_{ij}{}'(\theta, t) = N_{ij}W(\theta, t) + B_{ij} \tag{16}$$

where B_{ij} is the time-independent background random coincidence count rate. For source with random distribution of the direction of local fields (i.e. isotropic), the angular correlation $W(\theta, t)$ in Eq. (10) can be given by

$$W(\theta, t) = exp\left(-\frac{t}{\tau}\right)\{1 + A_2\gamma_a G_2(t)P_2(cos\theta)\} \tag{17}$$
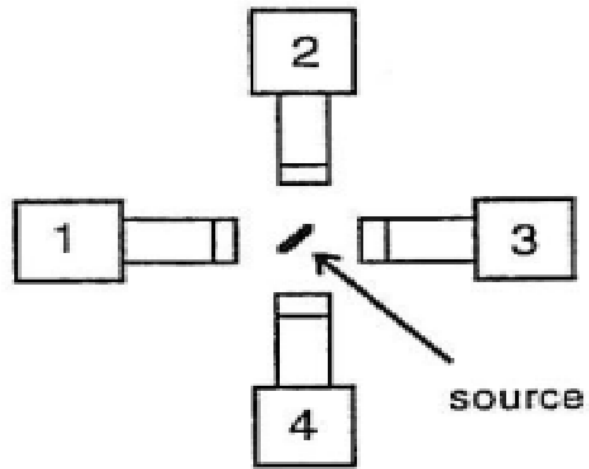
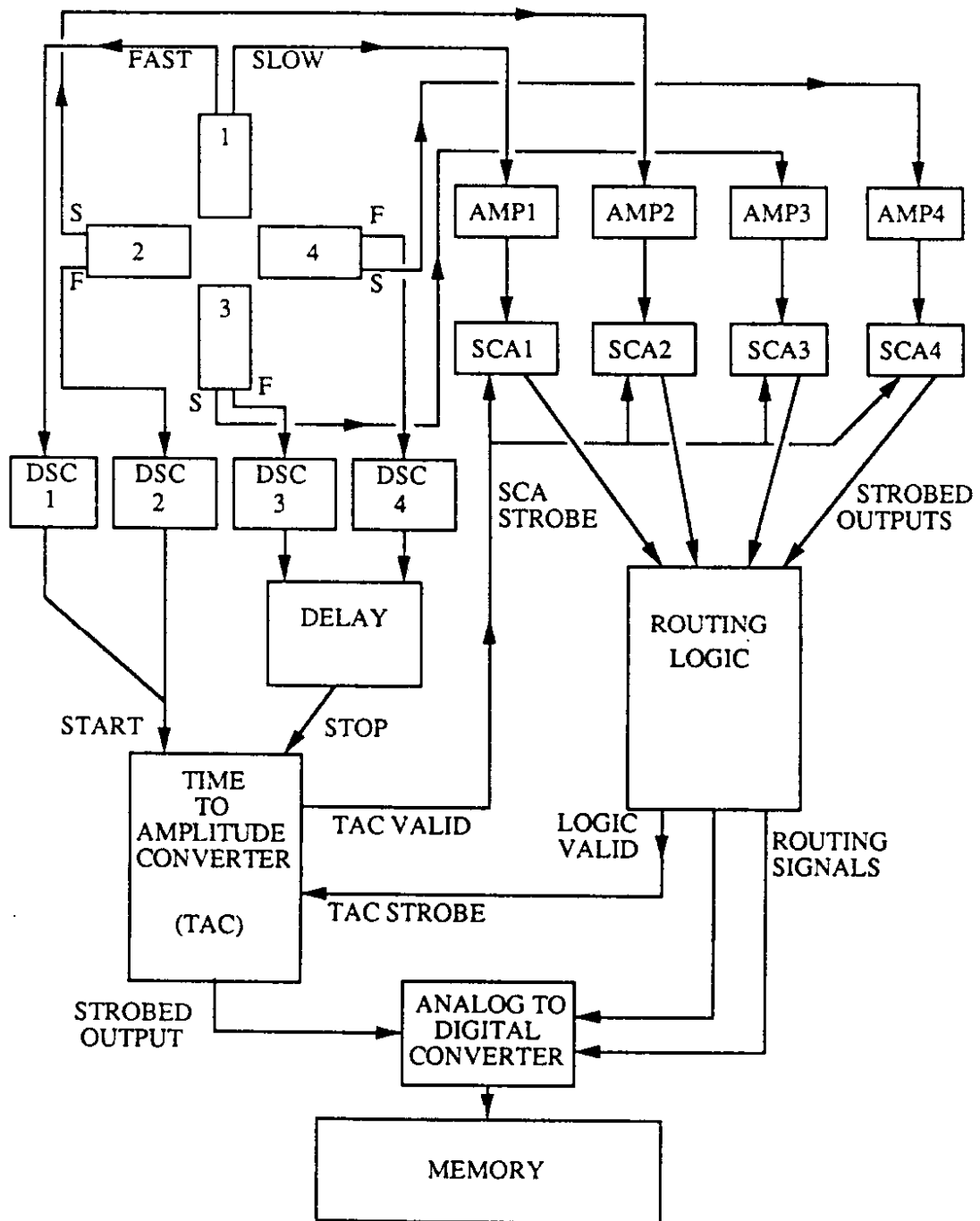Fig. 4. Geometrical arrangement of the detectors for a four detector PAC apparatus.

Fig. 5. Scheme of PAC experimental apparatus for a time-differential perturbed angular correlation measurement. (Taken from Ref. [9])

The perturbation function $G_{kk}(t)$ in section 2.1.3 can be expanded by Eq.(11). For nuclear spin $I = 5/2$ (Fig. 3), the parameters s_{2n} can be calculated and

$$G_2(t) = \frac{7}{35} + \frac{13}{35}\cos(\omega_0 t) + \frac{10}{35}\cos(2\omega_0 t) + \frac{5}{35}\cos(3\omega_0 t). \tag{18}$$

Here ω_0 equals to ω_Q^0 in eq.(11) and would be denoted as ω_1 in the following text.

In PAC experiments, $C_{ij}'(\theta, t)$ can be fit from the data collected, which is then subtracted from the background B_{ij} and gives the true coincidence count rate

$$C_{ij}(\theta, t) = C_{ij}'(\theta, t) - B_{ij}$$

here two geometric averages are used:

$$C(\pi, t) = \sqrt{C_{13}(\pi, t)C_{24}(\pi, t)}$$

$$C\left(\frac{\pi}{2}, t\right) = \sqrt{C_{14}\left(\frac{\pi}{2}, t\right) C_{23}\left(\frac{\pi}{2}, t\right)}$$

from Eq. (16) and Eq. (17), it can be easily shown that the experimental perturbation function $G_2(t)$ is given by

$$G_2(t) = \frac{2}{A_2 \gamma_a} \frac{C(\pi, t) - C\left(\frac{\pi}{2}, t\right)}{C(\pi, t) + 2C\left(\frac{\pi}{2}, t\right)} . \tag{19}$$

note that each of $C(\pi, t)$ and $C(\frac{\pi}{2}, t)$ are proportional to $\sqrt{\epsilon_1\epsilon_2\epsilon_3\epsilon_4\Omega_1\Omega_2\Omega_3\Omega_4}$, so that all those detector variables cancel in Eq. (19).

The solid angle attenuation factor γ_a is related to the experimental geometry of the four detectors, and in the present experiments it was approximately set as 0.7. If a probe nuclide has different nuclear environments, the total perturbation function will be a superposition of the perturbation functions

$$G_2(t) = \sum_i f_i G_{2i}(t)$$

The fractions f_i and perturbation functions $G_{2i}(t)$ can be fitted to the PAC spectra, and $\sum_i f_i = 1$.

2.3 Sample preparation

Samples of RPd$_3$ binary phases, R=La, Ce, Pr, Sm, Eu, Tb, Er, Yb, Lu, Sc and Y were prepared using the arc melting technique. In each phase, desired masses of two metals were cut from high purity metal foils. Then a razor blade was used to remove oxide from the surface of the metal pieces. Since rare earth metals easily become oxidized in air, the piece of rare earth metal was put in the mineral oil immediately after it was cleaned. Fresh carrier-free ^{111}In/Cd drops of activity dissolved in 0.05M HCl solution was placed on Pd metal in a few microliters each time and dried. Later, the rare earth metal was wrapped within the Pd metal and then they were put into an arc furnace for melting.

The melting was under argon gas atmosphere to avoid oxidation. During melt, the two pieces of metals shrank into a form of sphere which was shiny and metallic at first look after melt. The activity of the sample was then measured and a good value of it was determined using a scintillation detector to monitor. The mass of the sample after melt was weighted and the loss of mass was calculated by subtracting the weighted mass from the original mass. The composition range of the sample was determined by assuming that the mass loss was totally from either of the two components. Typical sample masses were from 45mg to 100mg and composition uncertainties ranged from 1 at % to 10.24 at % for different samples. Large mass losses occurred for some samples because rare earth metals tended to evaporate during melting. After melting, samples were either moved to PAC furnace for future experiments or else stored under mineral oil.

Binary phase RX$_3$ at the R-poorer boundary is denoted as boundary A, while RX$_3$ at the X-poorer boundary is boundary B. To make RX$_3$(A) or RX$_3$(B), the composition uncertainties need to be concerned and the full composition range of R should be completely larger than stoimetry for RX$_3$(A) or smaller for RX$_3$(B) phase.

Table 1. Composition ranges of rare-earth palladium phases. (Compositions were read from available binary phase diagrams in Ref. [18] at the lowest temperatures shown)

Phase	Minimum Pd-composition (at. %)	Maximum Pd-composition (at. %)
LaPd$_3$	-	-
CePd$_3$	75.2	80.6
PrPd$_3$	74.4	76.6
NdPd$_3$	74.9	74.9
SmPd$_3$	74.7	75.8
EuPd$_3$	74.9	74.9
TbPd$_3$	74.9	76.3
DyPd$_3$	75%	79
HoPd$_3$	74.9	76
ErPd$_3$	75.3	77
YbPd$_3$	75	-
LuPd$_3$	-	-
YPd$_3$	75	78.5
ScPd$_3$	75	75

In Fig. 6, a schematic rare-earth palladium phase diagram is shown, where a finite width of the phase field is indicated. Since the melting of metals would cause mass loss, it is unsafe to set the nominal composition inside the phase width because the real Pd-composition after melt cannot be judged farily due to the mass loss while only a Pd-composition range can be obtained. Therefore, to make a sample at the Pd-richer (poorer) boundary, it is necessary to make sure that the whole Pd-composition range is larger (smaller) than maximum (minimum) Pd-composition, sitting on the area A (B) as indicated in Fig. 6.
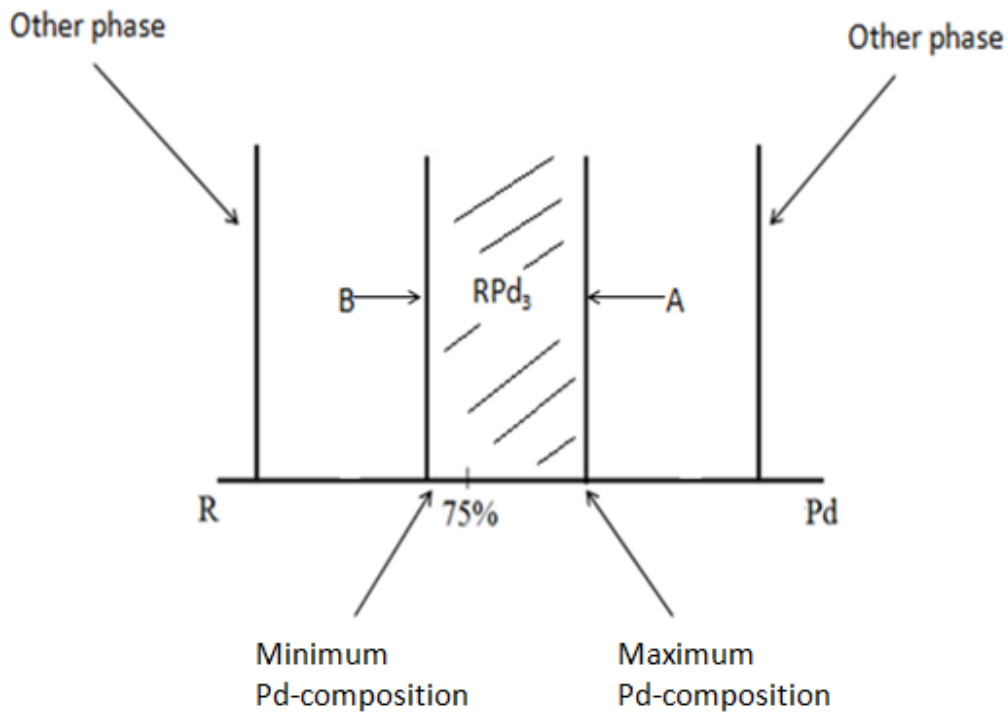

Fig. 6. Schematic phase diagrams of RPd_3. A and B denoted Pd-richer and Pd-poorer phase boundaries, respectively.

Chapter 3: Theory

3.1 Crystal Structure of L1$_2$ Phase

The crystal structure of L1$_2$ Phase is a face-center-cubic (fcc) based structure. For RPd$_3$ phase, rare-earth atoms are sitting on the corner points of the conventional unit cell (Fig. 1) while Pd atoms occupy face centers. The rare-earth atom has 12 nearest neighbor Pd atoms and the Pd atom has 4 rare-earth atoms and 8 Pd atoms neighbors.

The R site is cubic symmetric. However, the Pd site has tetragonal symmetry so that the EFG is axially symmetric and the principle axis is normal to the cubic face. Jumps of the probe atom between different sites cause reorientation of the EFG direction and damps out the perturbation function. The jump frequency of the probe atom w can be obtained from the fits of the perturbation functions which is proportional to the relaxation frequency λ [13].

3.2 Dynamical relaxation and inhomogeneous broadening

For phases A$_3$B with the L1$_2$ crystal structure (see Fig. 1), when ^{111}In probe atom occupies the Pd site, the EFG is axially symmetric and perpendicular to the face of the unit cell. The jumping of an ^{111}In probe atom between Pd sites will cause a reorientation of the direction of the EFG and thus the perturbation function will have dynamical damping which can be described by

$$G_2(t) = \exp(-\lambda t)\, G_2^{static}(t) \tag{20}$$

where $G_2^{static}(t)$ is the static perturbation function given in Eq. (19). The damping frequency λ can be related to the frequency of the change of the EFG due to the reorientation of the ^{111}In probe atom to one other orientation (w_{EFG}) [13]. There are two regimes in which the value of λ can be specified approximately,

$$\text{in slow fluctuation regime: } \lambda \cong (N-1)w_{EFG} \tag{21}$$

$$\text{in fast fluctuation regime: } \lambda \cong 100 \left(\frac{\omega_Q}{6}\right)^2 \left(\frac{1}{Nw_{EFG}}\right) \tag{22}$$

where ω_Q is the quadrupole interaction frequency and N is the number of different directions of the EFG. For L1$_2$ phase, $N = 3$ since it has three different orientations of the EFG, and hence $\lambda = 2w_{EFG}$. Moreover, In slow fluctuation regime, the jump frequency of ^{111}In probe atom w is

equal to the inverse mean residence time, $w = \frac{1}{\tau}$, which can be given by the product of the jump frequency of ^{111}In probe and the number of different EFG orientations, $w = 2w_{EFG}$. Therefore, $w = \lambda$ for the slow fluctuation regime (see also Ref. [13]).

However, the damping can also result from EFGs at the ^{111}In probe atom caused by defects on nearby sublattices, which is called the inhomogeneous broadening. Perturbation function $G_2(t)$ with inhomogeneous broadening is given by

$$G_2(t) = \frac{7}{35} + \frac{13}{35}\cos(\omega_0 t)\exp\left(-\frac{1}{2}\sigma t\right)$$

$$+ \frac{10}{35}\cos(2\omega_0 t)\exp(-\sigma t) + \frac{5}{35}\cos(3\omega_0 t)\exp\left(-\frac{3}{2}\sigma t\right) \qquad (23)$$

where $\omega_0 = 6\omega_Q$ and ω_Q is given by Eq. (14), and σ is the inhomogeneous broadening parameter depending on the distance of defects to the ^{111}In probe atom. Since it is hard to differentiate the damping from the dynamical relaxation and that from the inhomogeneous broadening, in the fitting of spectra one can reasonably assume that the dynamical relaxation can be ignored at room temperature, and thus the damping at room temperature is completely caused by inhomogeneous broadening. By fixing the σ obtained from room temperature spectrum, the dynamical damping factor λ could be fitted from higher temperature spectra.

3.2 Diffusion Mechanism and Point Defects in L1$_2$ phases

Several diffusion mechanisms are possible, including A-sublattice vacancy diffusion mechanism [4], a ring exchange mechanism [14], a B-vacancy six-jump cycle [15], a divacancy mechanism [16] and a vacancy conversion mechanism.

3.2.1 A-sublattice vacancy diffusion mechanism

A-sublattice vacancy diffusion mechanism might be the most elementary mechanism, which consider for In/Cd probe atom on the Pd site, there is a vacancy on the nearest Pd site and In probe atom can have random jumping to this vacancy. In a simple way, the total frequency should be a multiply of the number of nearest neighbor Pd sites z (z=8), the random jump frequency of In probe atom from one Pd site to the vacancy w_2 and the probability of vacancy on the Pd site $[V_{Pd}]$ (see Ref. [13]):

$$w = z[V_{Pd}]w_2 \tag{24}$$

and the diffusivity of In probe atom on Pd site is

$$D = \frac{1}{6}fd^2w \tag{25}$$

where d is the jump length ($d = \frac{1}{\sqrt{2}}a$ because of the fcc structure, a is the lattice constant) and f is the correlation coefficient for diffusion, which is a function of temperature in general cases. For self-diffusion of Pd on the Pd sublattice, f is equal to 0.689 [17].

3.2.2 Six-jump cycle mechanism

A six-jump cycle mechanism [15] describes a close loop jumping of a B-vacancy between A sites and B sites in A$_3$B phases. For RPd$_3$ phase, R-vacancy first jumps from the R site to the Pd site, then moves to another R site, passes through another Pd site and comes back to the original R site. However, to take into account the R-vacancy jumping between different R sites, the R-vacancy needs to make another two consecutive jumps to the other R site, which is called a six-jump cycle. During this process, two Pd atoms have been exchanged and the R-vacancy has switched its position with another R atom. The similar situation can be considered in the case of a Pd-vacancy, although the A-sublattice vacancy diffusion mechanism is probably much more effective.

3.2.3 Other Mechanisms

Ring exchange mechanism was first proposed by Zener [14] for bcc and fcc structures, where nearest neighbor sites are considered in a ring and probe atoms can jump in the ring with energy costs. For fcc structure, 3-ring and 4-ring diffusions are more favored than 2-ring diffusion because they cost less energy during probe atom jumping, and therefore are considered as more realistic in real diffusion.

The divacancy mechanism and the vacancy conversion mechanism are also possible diffusion mechanisms for L1$_2$ phases. In the divacancy mechanism [16], two near neighbor vacancies V_A and V_B form a divacancy and move at the same time while each of the vacancies stays on its own sublattice. In the vacancy conversion mechanism, a vacancy on one site can

react with another site to change to a vacancy on another site. For RPd$_3$, one of the reactions can be $V_R + In_{Pd} \rightarrow V_{Pd}:In_R$, and the new vacancy pair $V_{Pd}:In_R$ can contribute to the diffusion on the Pd sites. The jump frequencies of V_R and $V_{Pd}:In_R$ are of the same order without inhomogeneous broadening.

Chapter 4: Results

4.1 Heavy Rare Earth Palladium Phases RPd$_3$ (R=from Gd to Lu)

In this thesis, rare earth palladium phase RPd$_3$ at the R-poorer boundary and the Pd-poorer boundary are denoted as boundaries A and B, respectively. Heavy rare earth palladium phases (the lanthanide elements from Gd to Lu, and also Sc and Y) were prepared at both boundaries A and B, including R=Tb, Er, Yb, Lu, Y and Sc. Since these samples' spectra all show similar signals and the dynamical properties, only the spectra of LuPd$_3$ are shown provided here, i.e. LuPd$_3$ (A) and LuPd$_3$ (B).

The adjacent phases of LuPd$_3$ are Lu$_2$Pd$_5$ and pure Pd (Table 2). The sample LuPd$_3$(A) had nominal composition range of 19.3-20.4 at % Lu. The spectrum at $RT \cong 10°C$ (the left part of Fig. 7) showed a signal of site fraction 67(2) at % with a mean fundamental frequency $\overline{\omega_1} = 14.9(4)Mrad/s$. Another signal was an offset signal which had site fraction 31(1) at % at RT. These signals were due to the average of EFGs for In/Cd on the Lu-site affected by point defects located randomly in the lattice, probably Pd_{Lu} or V_{Lu}. As can be seen from the spectra of LuPd$_3$(A), the site fractions of the two signals were independent of the change of temperature.

Lu-Pd Crystal Structure Data

Phase	Composition, at.% Pd	Pearson symbol	Space group	Struktur-bericht designation	Prototype
(Lu)	0	$hP2$	$P6_3/mmc$	A3	Mg
LuPd(a)	50	$cP2$	$Pm\overline{3}m$	B2	CsCl
Lu$_3$Pd$_4$(b)	57.1	$hR14$	$R\overline{3}$	...	...
Lu$_2$Pd$_5$(c).......	71.4	$cF144$	$Fd\overline{3}m$	...	...
LuPd$_3$(d)	75	$cP4$	$Pm\overline{3}m$	L1$_2$	AuCu$_3$
(Pd)	100	$cF4$	$Fm\overline{3}m$	A1	Cu

(a) From [62Dwi]. (b) From [74Pal]. (c) From [74For]. (d) From [61Dwi].

Table 2. Crystal structure data of Lu-Pd system (taken from Ref. [18]).

Two LuPd$_3$ samples were made at the B boundary, including nominal composition ranges of (B1) 27.4-30.2 at % Lu and (B2) 24.4-30.2 at % Lu. Although the range of sample (B2) encompassed 25% (the stoichiometeric composition), this sample was determined to be at the B-boundary (Pd-poorer) because a high frequency $\omega_1 \approx 107\ Mrad/s$ was identified at room temperature (RT) as sample B1, while this high frequency can also be seen in other heavy lanthanide palladides at the B-boundary. The spectrum at RT (the right part of Fig. 7) fitted with a majority high frequency of site fraction 70(1) at % with $\omega_1 = 107.4(2)Mrad/s$, an inhomogeneious broadening $\sigma = 2.5(2)Mrad/s$ and a offset signal of site fraction 23.9(5) at %. The high frequency was attributed to ^{111}In/Cd probe on the Pd-site of LuPd$_3$. As temperature increased, the high frequency did not have dynamical relaxation even at $T \approx 1200K$. Also, no obvious dependence of site preference on temperature was observed for LuPd$_3$(B) samples (as well as other heavy rare earth palladium L1$_2$ phases RPd$_3$, whose spectra are not shown in this thesis).
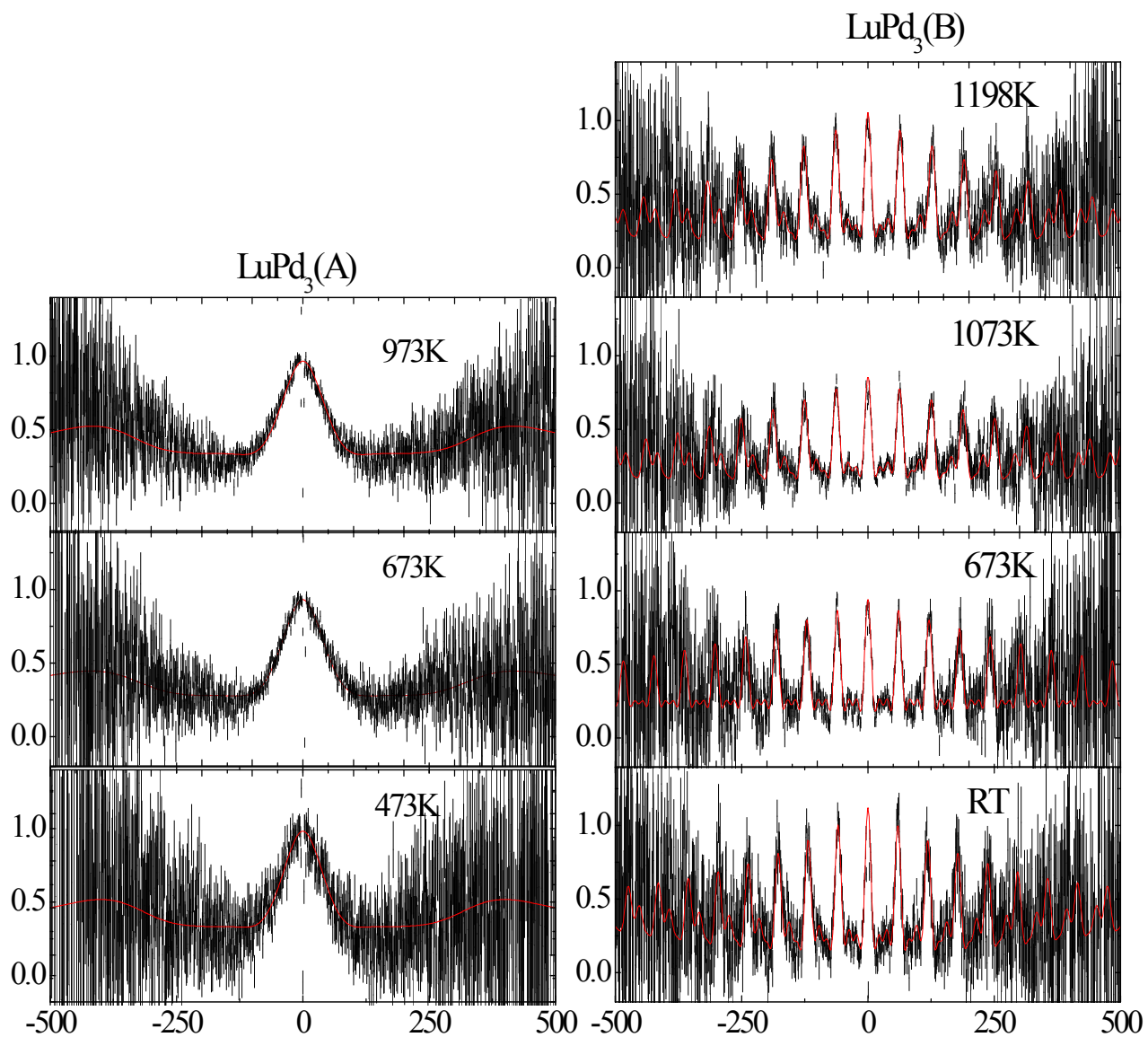
Fig. 7. PAC spectra of LuPd$_3$ at the opposing boundaries A and B. Solid lines are best fits of perturbation function to Eq. (20). (Data of LuPd$_3$ (B) taken from the B1 sample)

4.2 Intermediate Weight Rare-Earth Palladium Phases RPd$_3$ (R=Pr, Nd, Eu and Sm)

Jump frequencies and site preference of PrPd$_3$ were measured for both boundaries A and B. The adjacent phases of PrPd$_3$ are Pd$_5$Pr and Pd$_2$Pr (Fig. 8). The sample PrPd$_3$(A) had nominal composition range of 20.3-21.3 at % Pr. This sample showed a majority signal of offset with site fraction 58(1) at % at RT and a minority signal of $\overline{\omega_1} = 6.4(4) Mrad/s$ with site fraction 32(1) at % at RT (Fig. 16). The offset signal was attributed to ^{111}In probes at the Pr site and the low frequency signal was caused by the EFG from Pd_{Pr} or V_{Pr} defects at the SNN Pr site. As temperature increased, the site fractions of the offset signal became larger, as can be seen from the flatter spectrum at higher temperature. This behavior may be due to the reorientation of the EFG caused by the jumping of random Pd_{Pr} or V_{Pr} point defects located near ^{111}In/Cd probe.
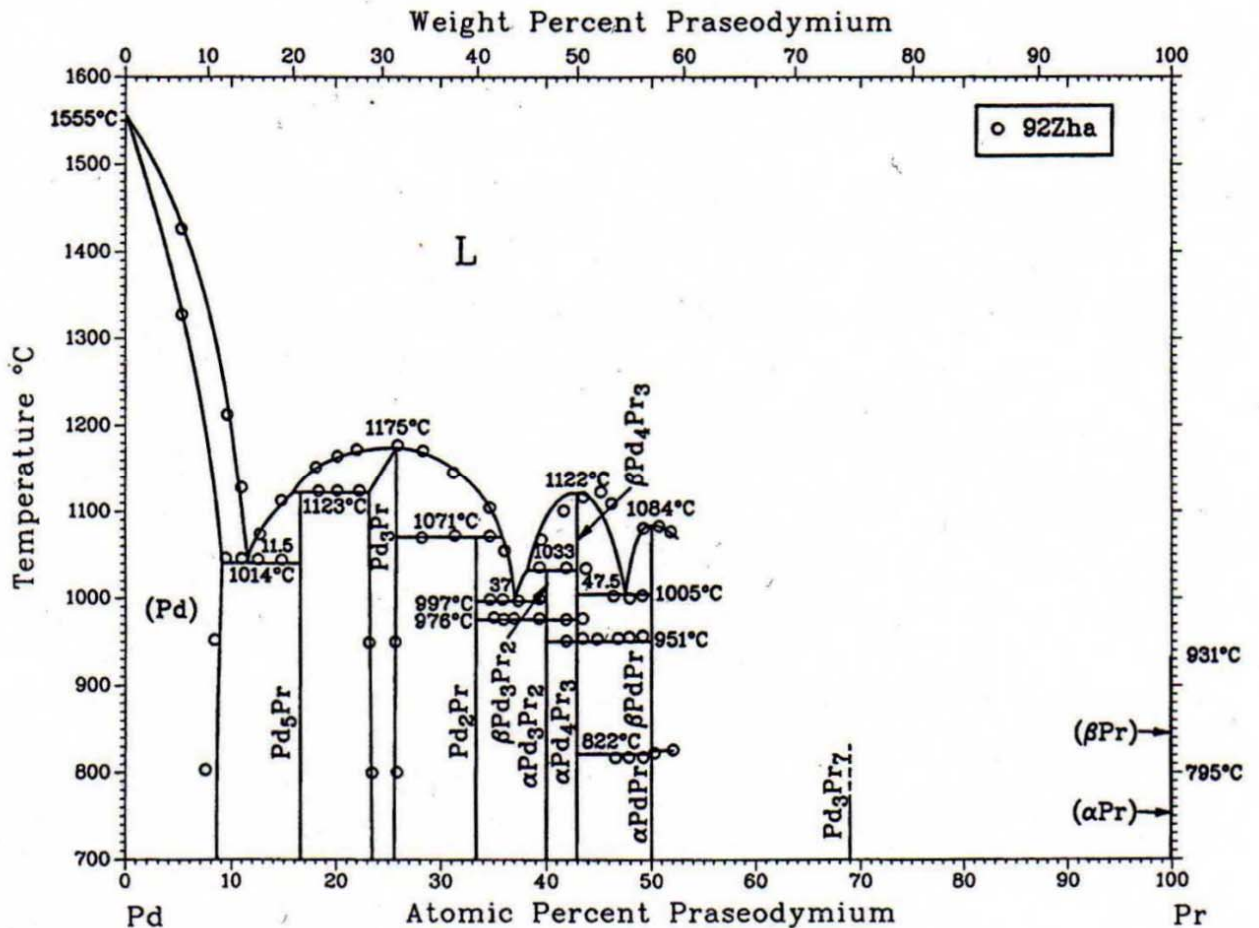
Fig. 8. Phase diagram of Pd-Pr system (taken from Ref. [19])
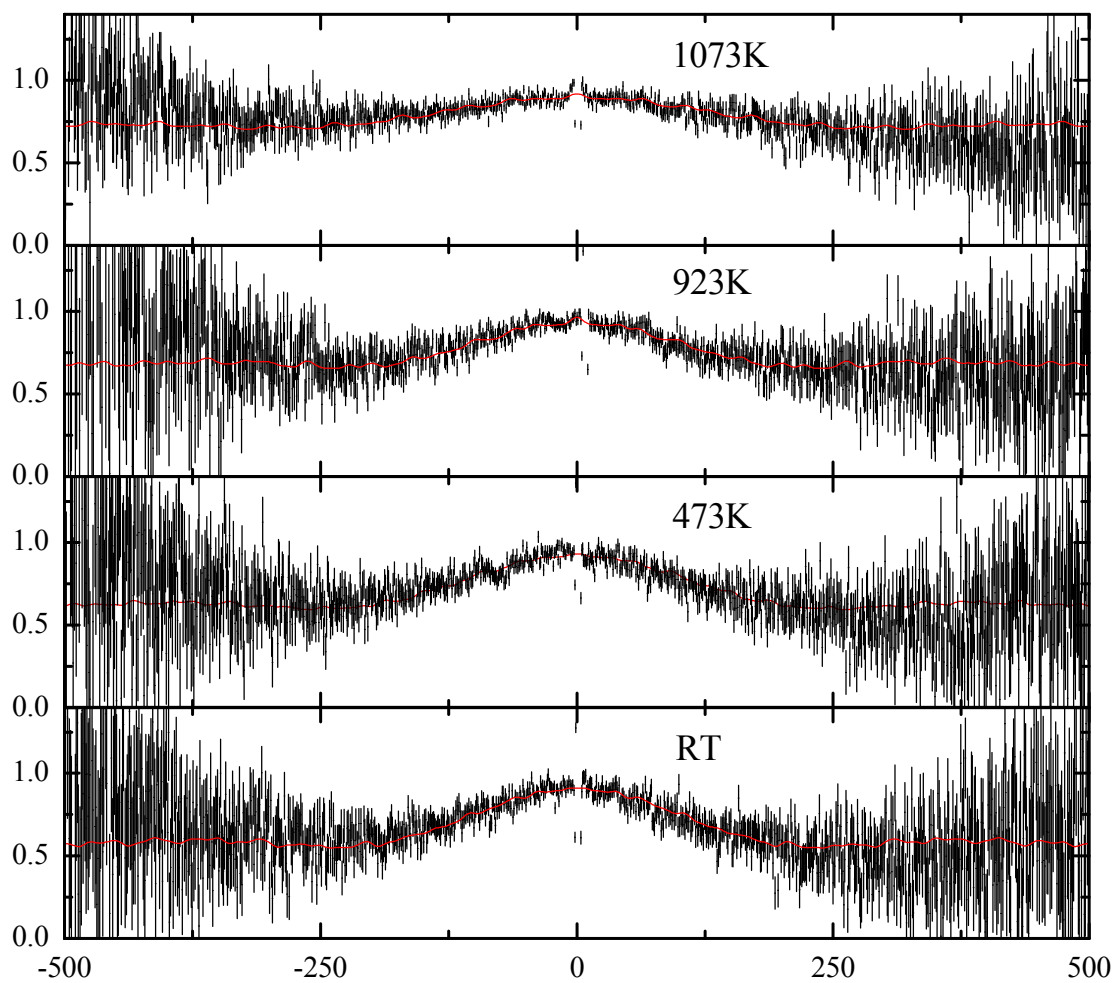
Fig. 9. PAC spectra of PrPd$_3$(A). Solid lines are best fits of perturbation function.

The sample PrPd$_3$(B) had nominal composition range of 26.3-27.2 at % Pr. Fig. 10 shows representative PAC spectra of the PrPd$_3$(B) in the slow fluctuation region fitted with Eq. (20) for the perturbation functions (solid lines). The fit at RT had a majority signal of site fraction 68(1) at % with the fundamental frequency $\overline{\omega_1} = 119.3(1) Mrad/s$, which was axially symmetric. The majority signal was attributed to ^{111}In/Cd probes on the Pd-sublattice of PrPd$_3$. The spectrum at RT also had an offset signal of site fraction 19.9(5) at %. The low frequency can be attributed to ^{111}In/Cd probes on the Pr-sublattice of PrPd$_3$ with EFG from the defects at the SNN sublattice. Also, one can attribute the offset signal to ^{111}In/Cd probes on the Pr-sublattice of PrPd$_3$. As temperature increased, the spectra showed temperature dependence of site preference, i.e. the offset site fraction decreased while the site fraction of site fraction increased, showing that ^{111}In/Cd probes tended to move to Pd-sublattice at higher temperatures. Theoretically, the ratio of the site fractions f(Pr)/f(Pd) should satisfy the thermal equilibrium equation [9]:

$$In_R + Pd_{Pd} \leftrightarrow Pd_R + In_{Pd} \ \text{ or } \ In_{Pd} + R_R \leftrightarrow R_{Pd} + In_R$$

$$\frac{f(R)}{f(Pd)} = r_0 \exp\left(\frac{Q}{k_B T}\right) \tag{26}$$

$$= \frac{1}{3}[Pd_R] \exp\left(-\frac{S_{xfer}}{k_B}\right) \exp\left(\frac{Q}{k_B T}\right)$$

$$\text{or } = \frac{1}{3}\frac{1}{[R_{Pd}]} \exp\left(-\frac{S_{xfer}}{k_B}\right) \exp\left(\frac{Q}{k_B T}\right)$$

where S_{xfer} and Q are the change in vibrational entropy and enthalpy when ^{111}In/Cd probe transfers from the R site to the Pd site. The bracketed quantity $[R_{Pd}]$ is the fraction of Pd-sublattice occupied by rare-earth atoms, $[R_{Pd}] \equiv N_{Pd}^R / N_{Pd}$, where N_{Pd}^R is the number of Pd-sites occupied by species R, and N_{Pd} is the total number of Pd-sites. Fig. 11 shows the fit of ratio plot for R=Pr with Eq. (26), where the slope of fit is 0.5 eV. For Pr composition far from the stoichiometric value, the majority of Pr_{Pd} defects would be thermally activated and $[Pr_{Pd}]$ is approximately independent of temperature [3], and therefore one can attribute the slope to the transfer enthalpy Q. In Fig. 17 one can see two regions have been identified, while at low temperatures system cannot reach equilibrium states and thus ratio points deviate from the fit. In this sample PrPd$_3$(B), the transfer enthalpy $Q \approx 0.5(1) \ eV$.

The fit of the values of λ (equals to jump frequency w) to Eq. (20) is shown in Fig. 16 (b). The six measurements at high temperature fall in a straight line while the three deviated measurements may be due to the effect of inhomogeneous broadening. The activation enthalpy can be obtained from the slope of the fit, $Q = 0.8(2) eV$.
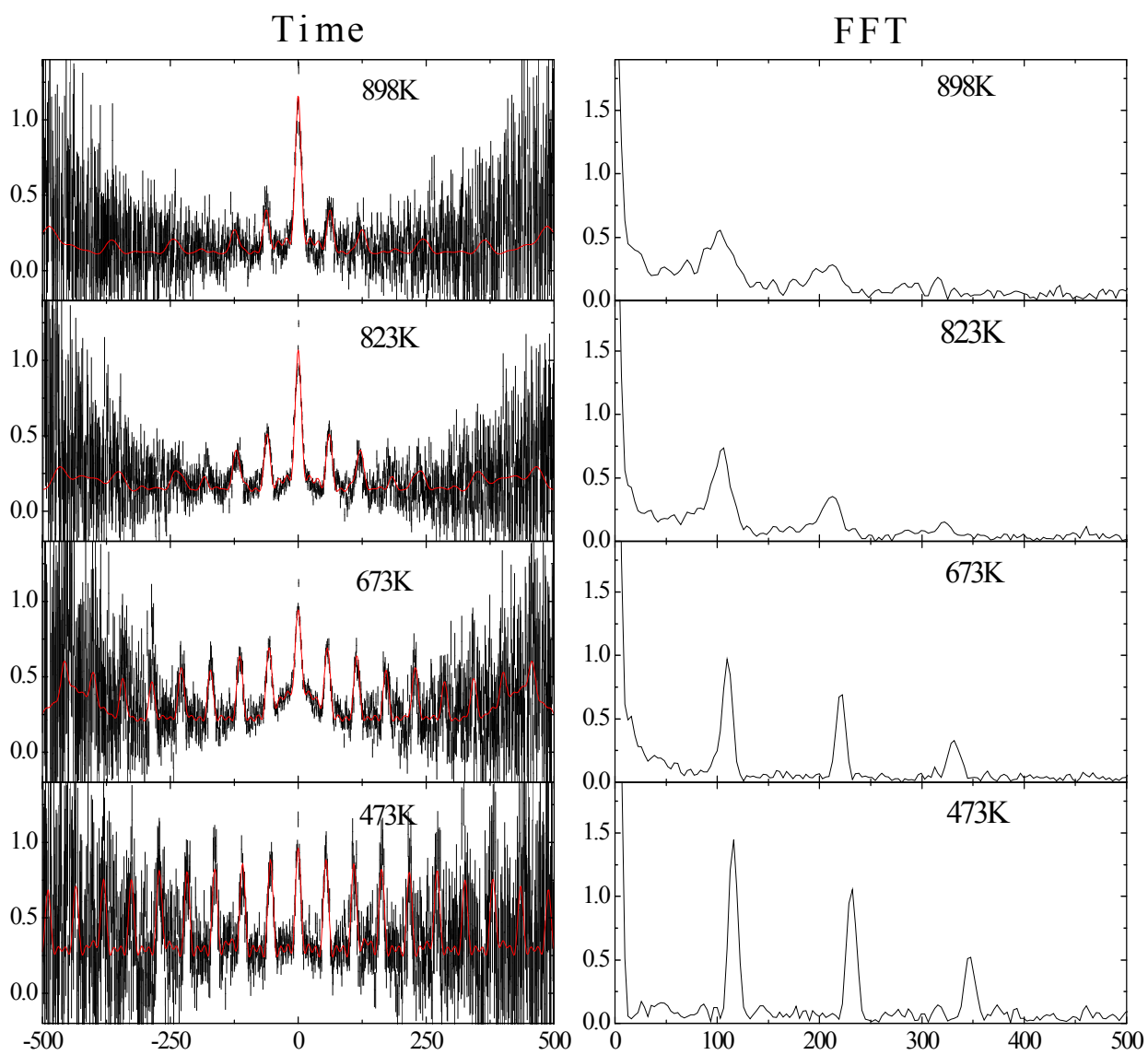
Fig. 10. PAC spectra of PrPd$_3$(B). The left part shows the time domain spectra where solids lines are best fits to Eq. (20) and the right part is the FFT of the time spectra

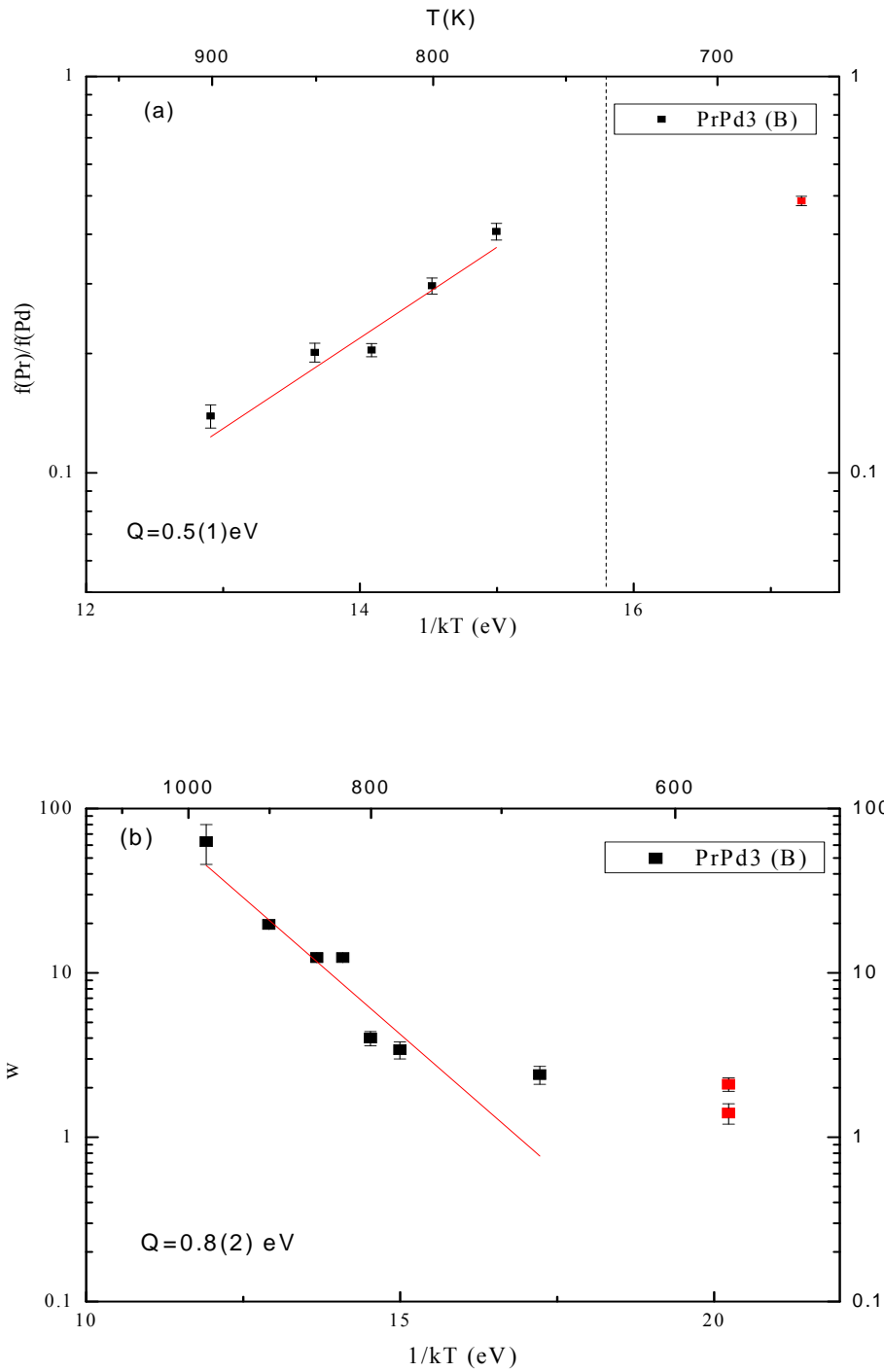Fig. 11. (a) Ratio of site fractions f(Pr)/f(Pd) and (b) jump frequencies of In/Cd, plotted versus inverse temperature for PrPd$_3$(B). Straight lines show fits to Eq. (26) for (a) and Eq. (20) for (b). Dash line separates equilibrium region and non-equilibrium region.

Results of R=Nd, Sm and Eu at the A boundary would be ignored here because they had similar signals and behaviors as the heavy rare earth palladium $L1_2$ phases in section 4.1.

The adjacent phases of $NdPd_3$ are $NdPd_5$ and Nd_3Pd_4 (Fig. 12). Sample $NdPd_3$(B) had a nominal composition range from 29.0-30.8 at % Nd. The spectrum at RT showed a high frequency $\omega_1 = 110.5(1) Mrad/s$ with site fraction 59(1) at % and an offset signal with site fraction 14.7(3) at %. As temperature increases, the high frequency started to show dynamical relaxation above 673K (see Fig. 13), and at temperatures above 1100K this frequency was completely damped whose amplitude cannot be seen in the Fast Fourier Transformation (FFT) spectrum. In a further step, the small change of site fractions of the signals with temperature was also studied (Fig. 14) and the ratio of site fractions f(Nd)/f(Pd) slightly increases as temperature goes from low to high. Therefore, the transfer enthalpy Q=0.32(9) eV.
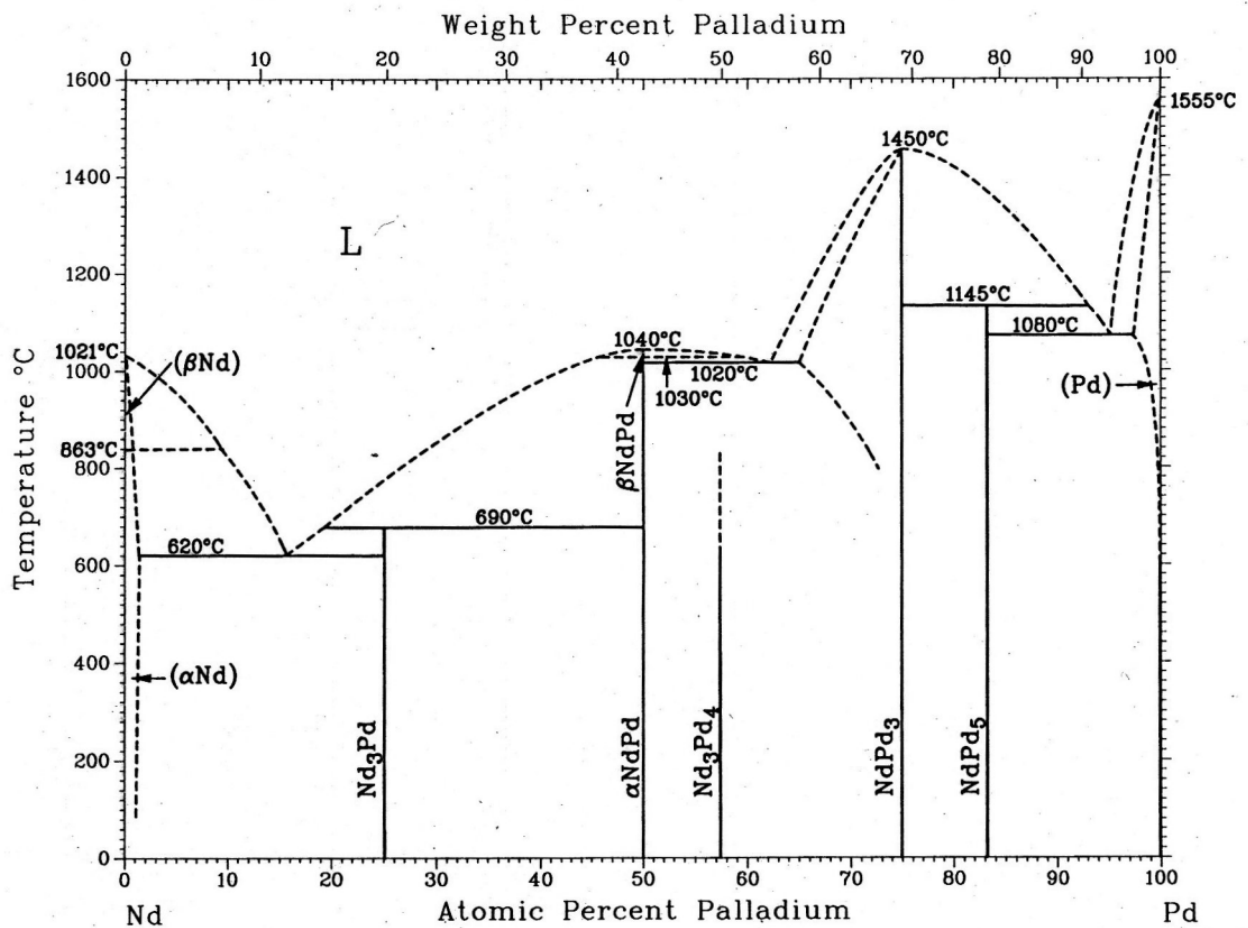
Fig. 12. Crystal structure data of Nd-Pd system (taken from Ref. [18])
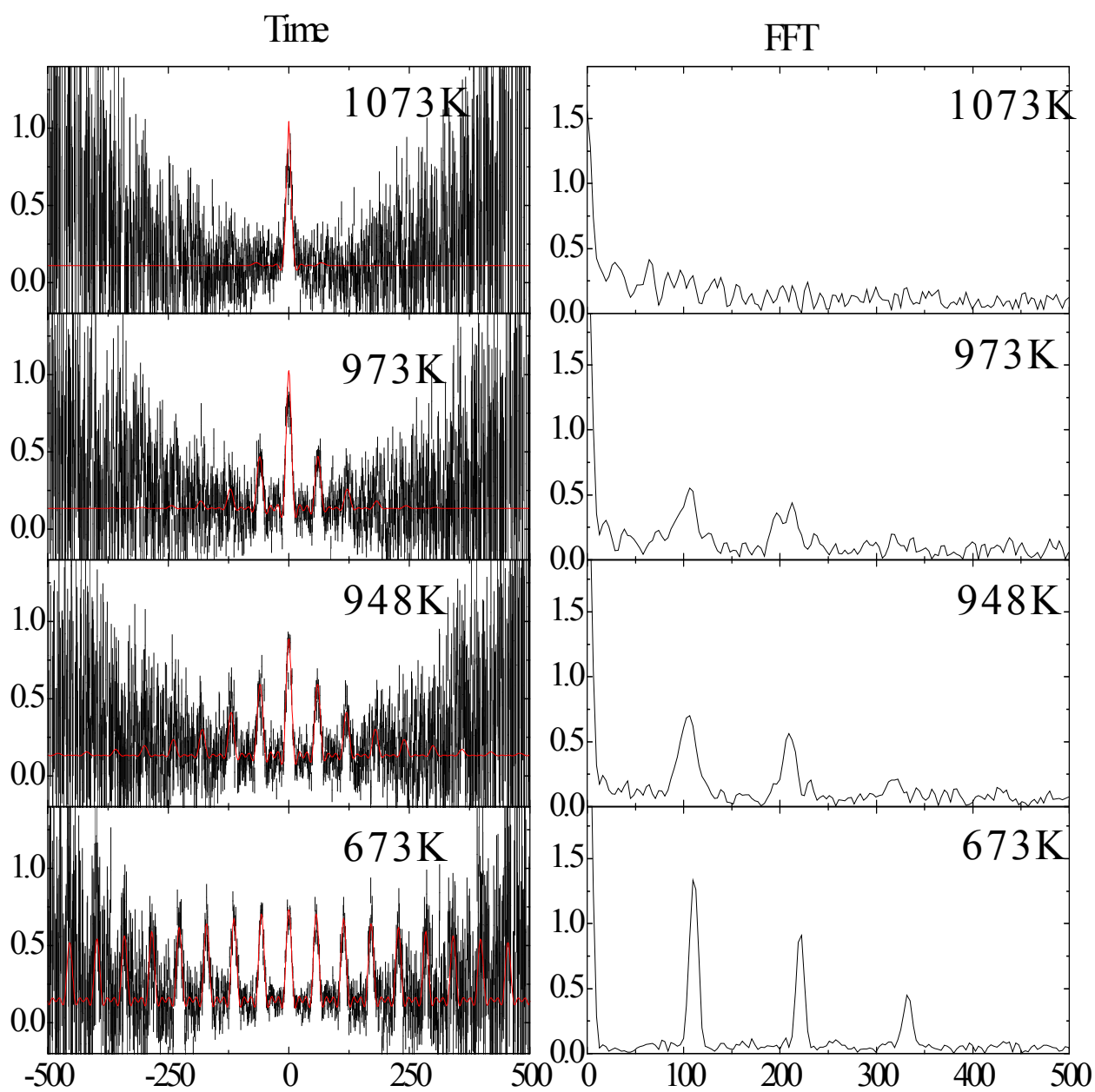
Fig. 13. PAC spectra of NdPd$_3$(B). The left part shows the time domain spectra where solid lines are the best fits to Eq. (20) and the right part is the Fast Fourier Transformation (FFT) of the time spectra.
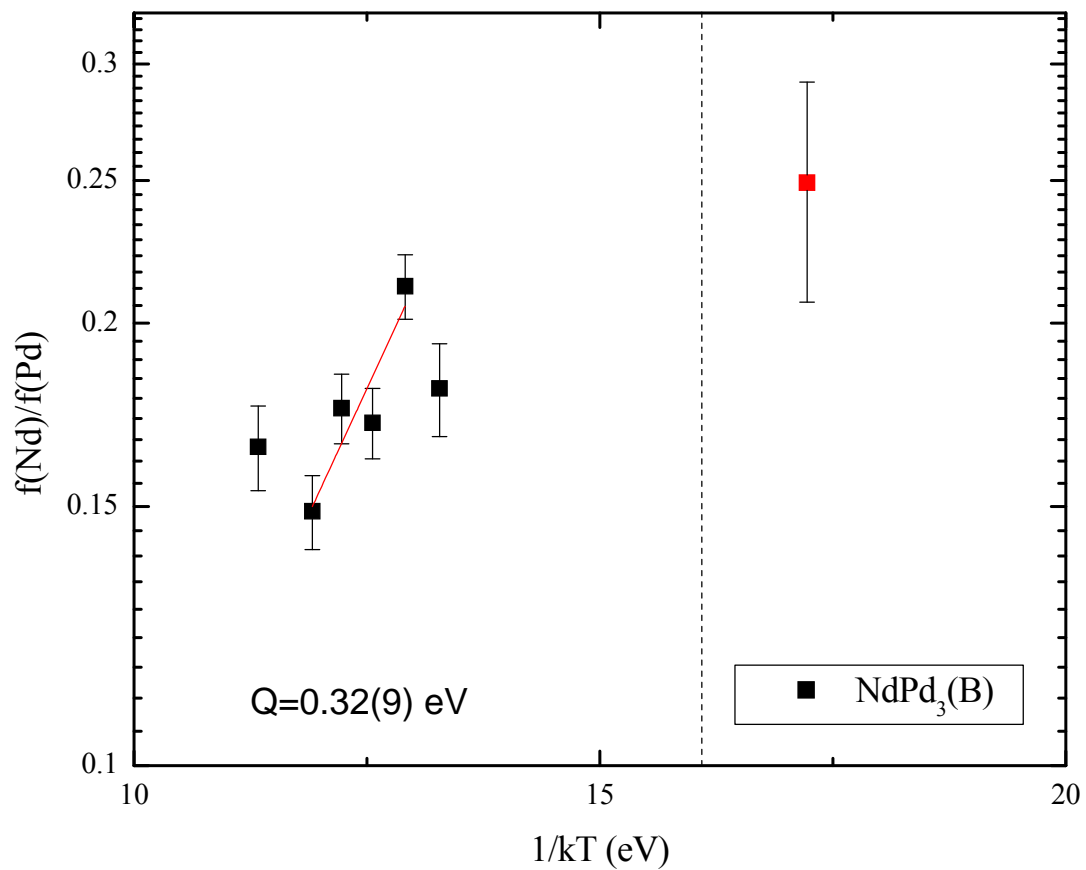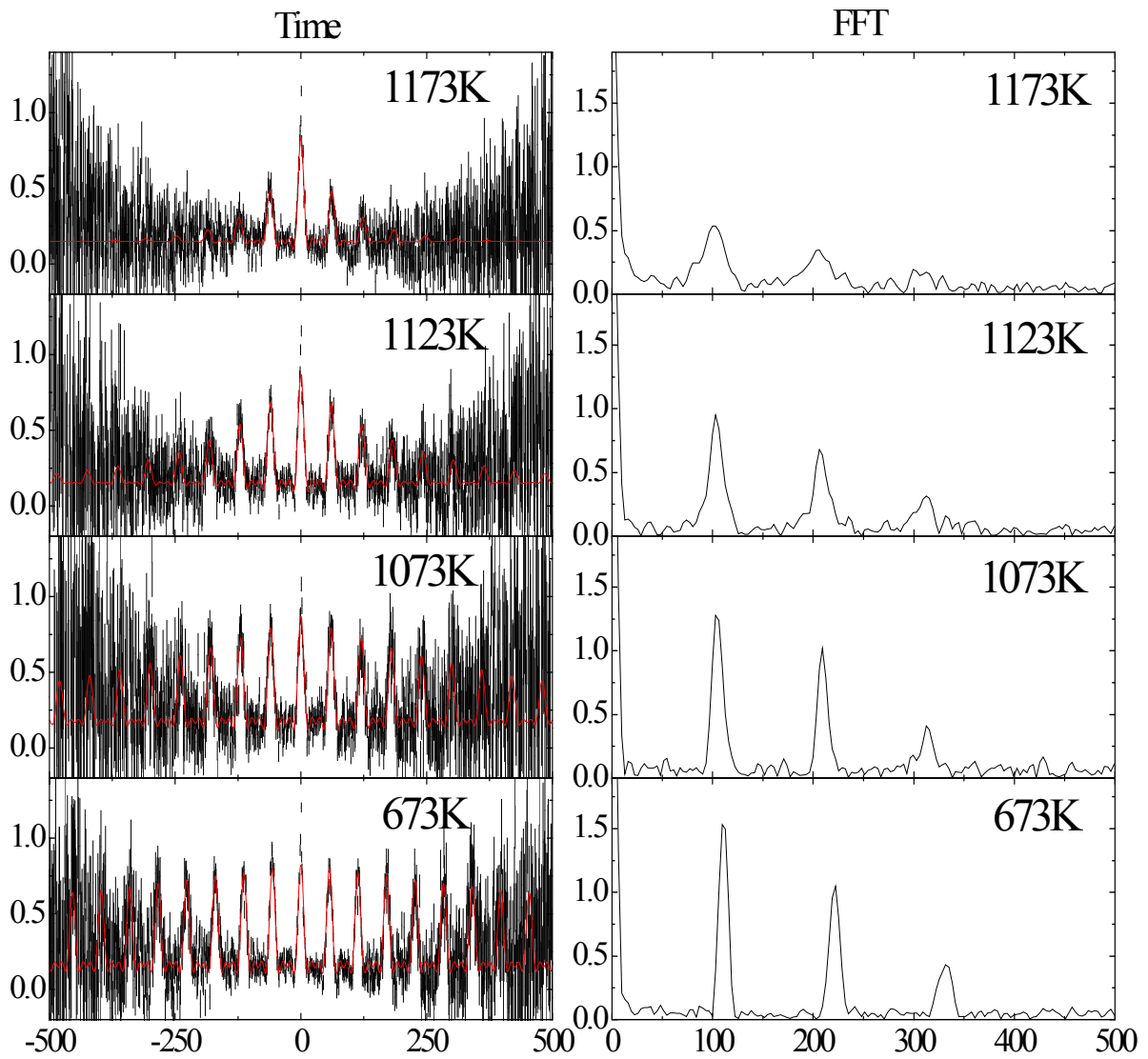
Fig. 14. Ratio of site fraction of In on Nd-site over site fraction of In on Pd-site for NdPd$_3$(B), plotted versus inverse temperature. Solid line is fit to Eq. (26). Dash line separates equilibrium region and non-equilibrium region.

SmPd$_3$ has adjacent phases Pd$_5$Sm and Pd$_{21}$Sm$_{10}$ (Fig. 15). The sample SmPd$_3$(B) had nominal composition range of 27.2-37.5 at % Sm. In PAC spectra, SmPd$_3$(B) had similar signals as NdPd$_3$, a high frequency $\omega_1 = 116.54(9) Mrad/s$ with site fraction 62(1) at % and an cubic signal (offset) with site fraction 11.7(2) at % at RT. The temperature where SmPd$_3$(B) starts to show dynamical relaxation (Fig. 16), was higher than that of NdPd$_3$(B) proving that SmPd$_3$(B) had larger activation enthalpy. As temperature increased, the high frequency's site fraction dropped while the site fraction of cubic signal increased (Fig. 17). The transfer enthalpy of SmPd$_3$(B) is Q= -0.07(2) eV.
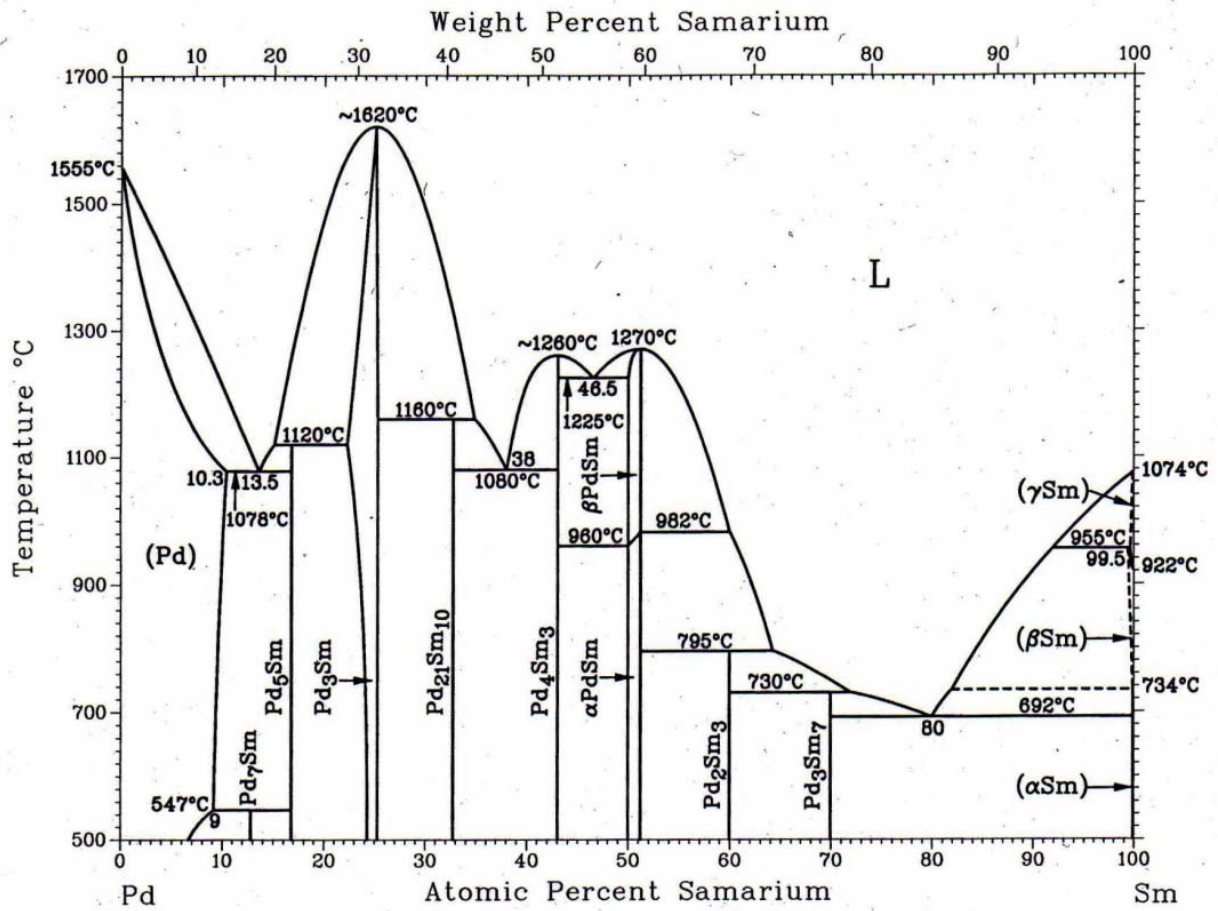
Fig. 15. Phase diagram of Pd-Sm system (taken from Ref. [18])

Fig. 16. PAC spectra of SmPd$_3$(B). The left part is shows the time domain spectra where solid lines are best fits to Eq. (20) and the right part is the FFT of the time spectra.
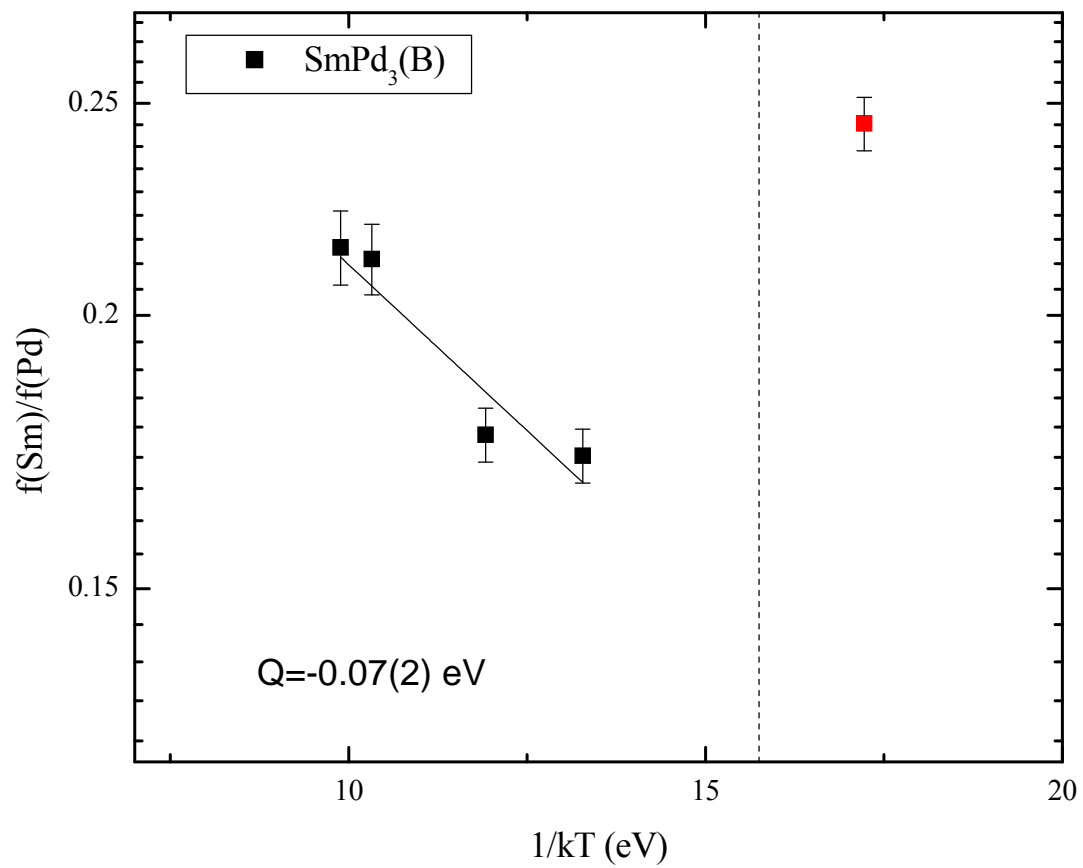
Fig. 17. Ratio of site fraction of In on Sm-site over site fraction of In on Pd-site, plotted versus inverse temperature. Solid line shows fit to Eq. (26). Dash line separates equilibrium region (left) and non-equilibrium region (right).

EuPd$_3$ was also studied because it had lattice constant between NdPd$_3$ and SmPd$_3$. The adjacent phases of EuPd$_3$ are EuPd$_5$ and EuPd$_2$ (Fig. 18). The sample EuPd$_3$(B) had nominal composition range of 24.7-33.6 at %Eu. For the two signals, the high frequency $\omega_1 = 117.1(3)Mrad/s$ had site fraction 53(2) at % at RT while the offset signal had site fraction 37.7(4) at %. The high frequency of EuPd$_3$(B) was close to frequencies in other RPd$_3$ phases, unlike in stannides RSn$_3$, where EuSn$_3$ has frequency as half as other RSn$_3$ phases.

The dynamical relaxation of EuPd$_3$(B) is shown in Fig. 20 and one can see that the activation enthalpy of EuPd$_3$(B) is between that of NdPd$_3$(B) and SmPd$_3$(B) because its dynamical damping happens at an intermediate temperature. This behavior strongly suggests that the activation enthalpy of RPd$_3$ should be related to its lattice constant (see also section 5.1). As temperature increases from 673K to 1173K, the site fraction of the high frequency drops while at the same time the offset signal increases, which can be plotted versus inversus temperature (Fig. 19). Theoretically, ^{111}In tracers switch from Pd site to Eu site can be described as

$$In_{Pd} + Eu_{Eu} \leftrightarrow Eu_{Pd} + In_{Eu}$$
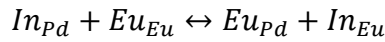
The site-ratio of f(Eu)/f(Pd) can be given by

$$\frac{f(Eu)}{f(Pd)} = \frac{1}{3[Eu_{Pd}]} \exp\left(-\frac{S_{xfer}}{k}\right) \exp\left(\frac{Q}{kT}\right) = r_0 \exp\left(\frac{Q}{kT}\right) \tag{26}$$

The first several points which deviated from the fit line may be because these points were at low temperatures where equilibrium had not been set up. The transfer enthalpy fitted was Q= -0.14(1) eV (Here the enthalpy was obtained by averaging the two transfer enthalpies). As can be seen, the increase of the ratio with temperature indicated that ^{111}In prefers to switch from the Pd-site to the Eu-site at higher temperatures.
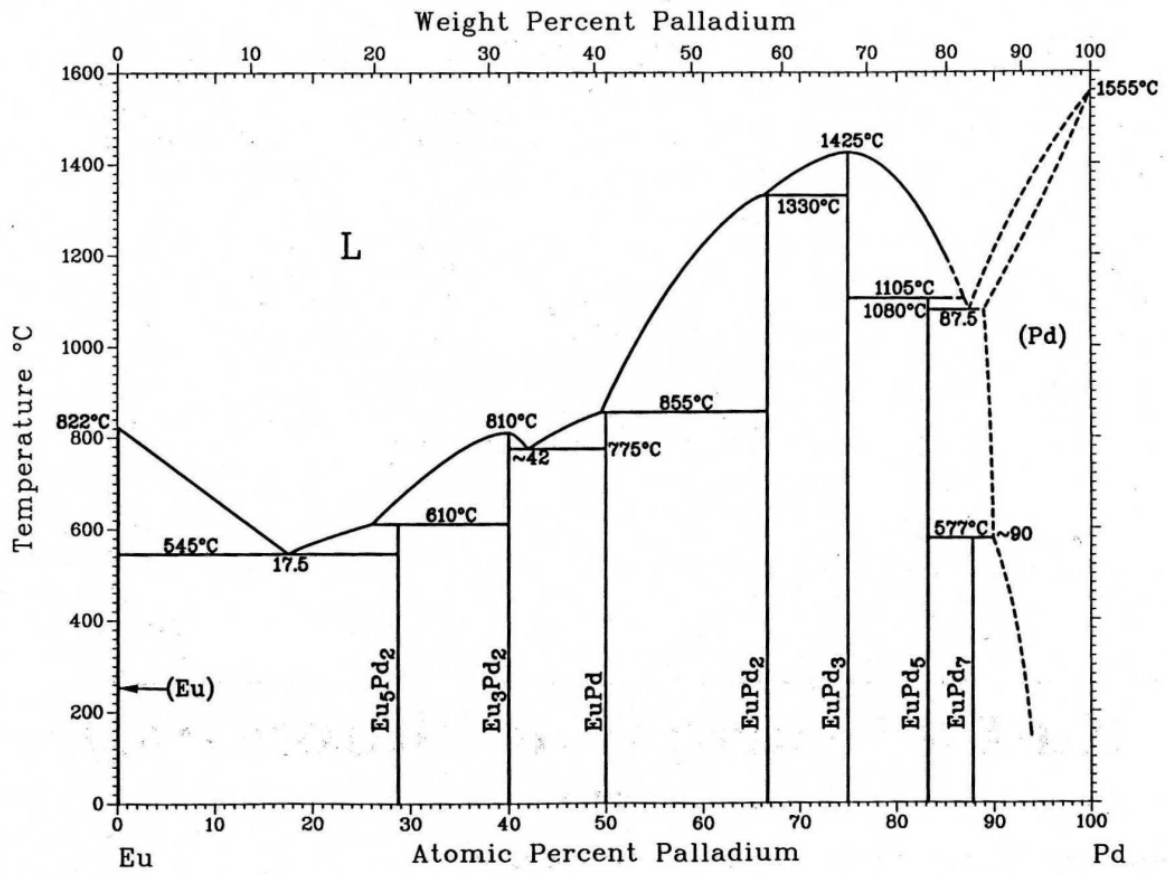
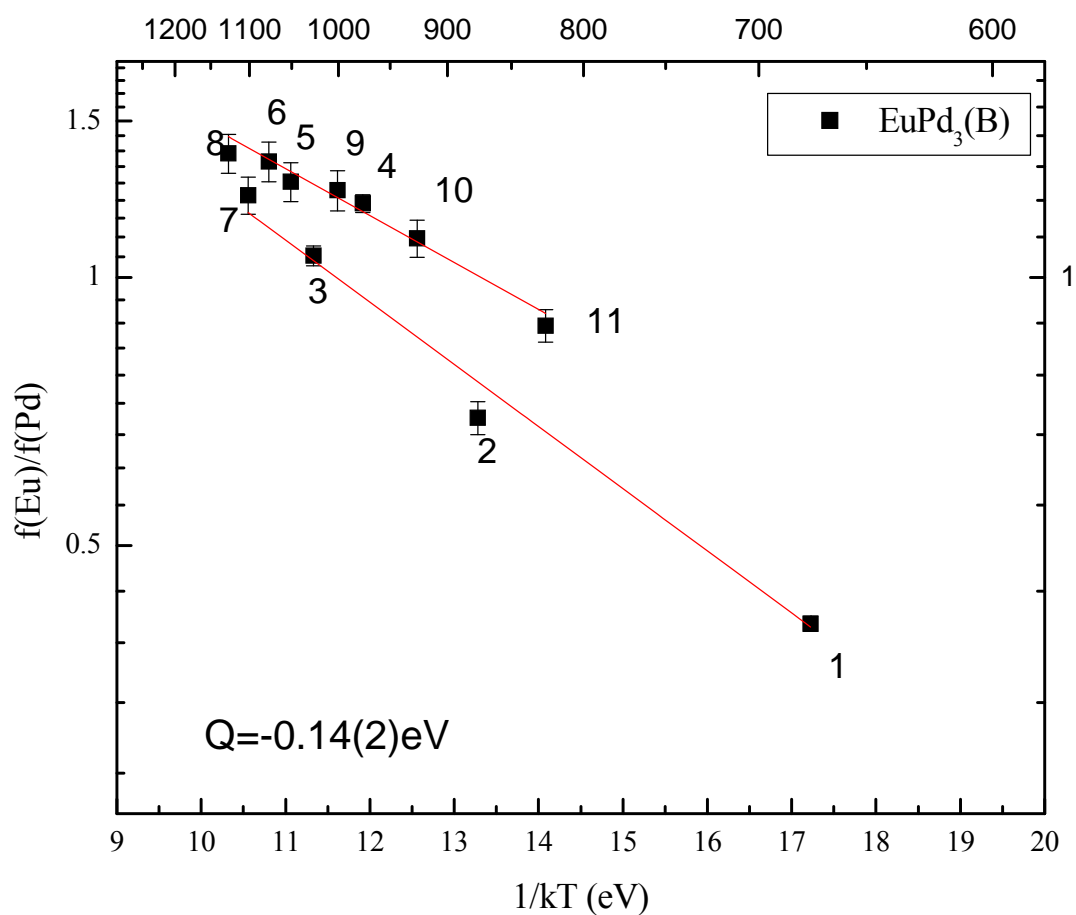Fig. 18. Phase diagram of Eu-Pd system (taken from Ref. [18])

Fig. 19. Ratio of site-fraction of ^{111}In on Eu-site over site-fraction of ^{111}In on Pd-site. Solid lines are fit to Eq. (26). Numbers are in the order of measurement. Activations enthalpy is obtained from the average of the two fits.
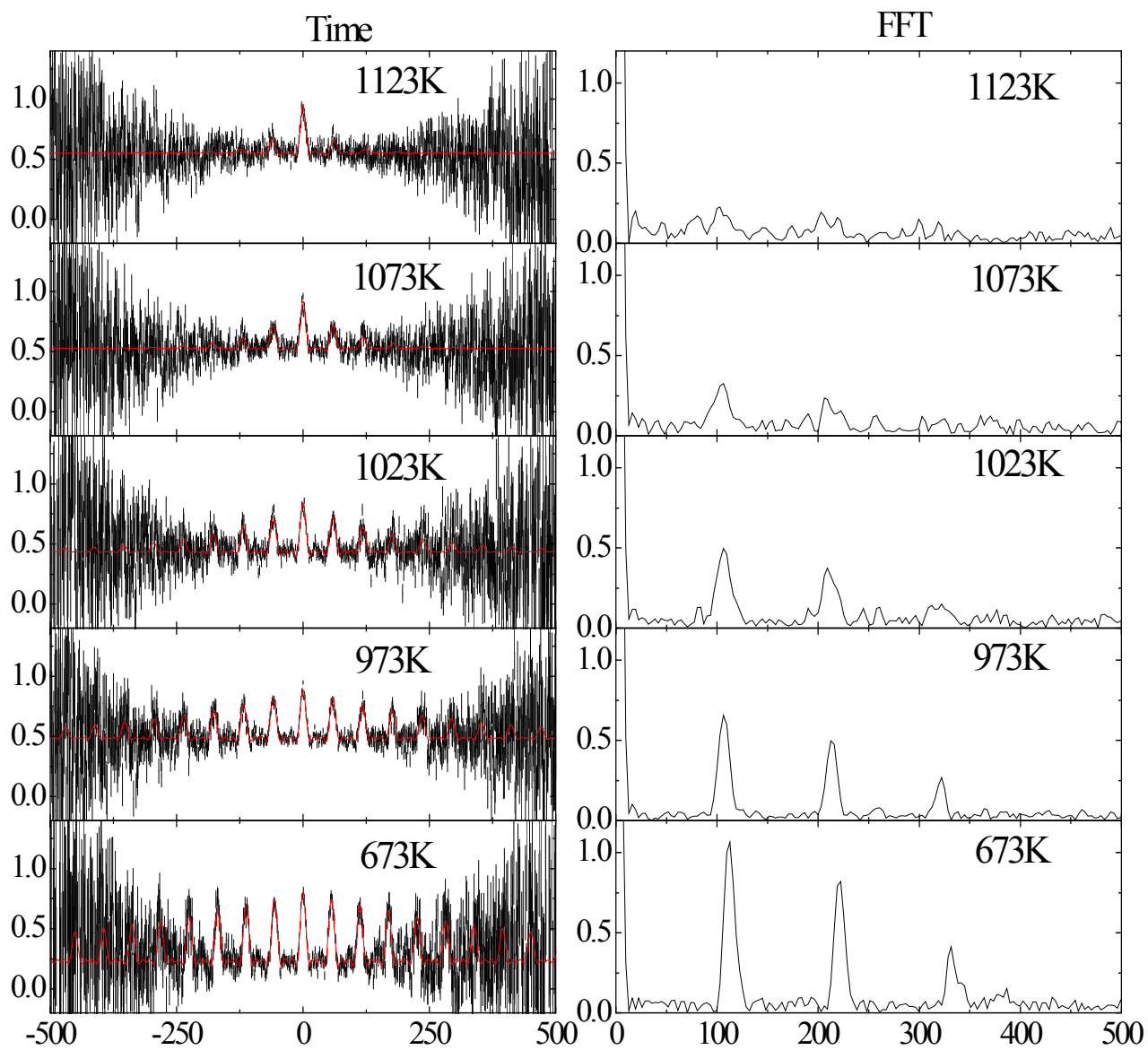
Fig. 20. PAC spectra of EuPd$_3$(B). The left part shows the time domain spectra where solid lines are best fits to Eq. (20) and the right part is the FFT of the time spectra.

4.4 Light Rare-Earth Palladium Phases RPd$_3$ (R=La and Ce)

LaPd$_3$ samples were prepared at both phase boundaries A and B. The adjacent phases of LaPd$_3$ are pure Pd and La$_3$Pd$_4$ (Table 3).

Sample LaPd$_3$(A) had nominal composition range of 19.1-20.4 at % La, which was at the A boundary (La-poorer). The left portion of Fig. 22 shows representative PAC spectra of the LaPd$_3$(A) sample from room-temperature (RT) to 673K. The solid lines were perturbation functions fitted with Eq. (20). The fit of the spectrum at RT had a signal of 20(1) at % site fraction with a mean fundamental frequency $\overline{\omega_1} = 7.9(9)Mrad/s$, and a offset signal of 38(4) at % site fraction with $\omega_1 = 129(2)Mrad/s$ and $\eta = 0.44(1)$ (here η is not the η in Eq. (9)). The minority signal was attributed to the EFG from defects surrounding the probe ^{111}In/Cd atoms. The non-axially symmetric majority signal did not come from LaPd$_3$ because there are no non-axially symmetric sites in this phase. X-ray measurement showed that there was another phase LaPd5 in this sample which is believed to be a D2$_d$ structure (Prototype CaCu$_5$) [27]. In this phase, there are two different types of Pd-sites, one is symmetric while the other is non-axially symmetric. The high frequency in this phase must be from the non-axially symmetric Pd-site. The 33(1)% fraction of offset in the spectra could be attributed to probes which occupy the R-site in the L1$_2$ structure.

The nominal composition range of LaPd$_3$(B) sample was 26.4-28.0 at %La, definitely at the B boundary (La-richer). The spectra (the right part of Fig. 21) fitted with only two signals. The dominant signal was the offset signal, with 63(2) at % site fraction at RT. This offset signal was reasonably attributed to ^{111}In/Cd probes at the La-site, where EFG is zero because in cubic symmetric La-site quadrupole interaction frequency is $\omega_1 = 0$. The general rule is that in Pd-poorer sample ^{111}In/Cd probes would like to occupy Pd-site, while in this phase ^{111}In/Cd occupied R-site instead of Pd-site. The minority signal was a mean frequency signal, $\overline{\omega_1} = 5.0(4)Mrad/s$ with 38(2) at % site fraction at RT. This signal should be from the average of EFGs from random defects e.g. Pd atom at SNN La-site (Pd_{La}) or vacancy at SNN La-site(V_{La}). As temperature increased, the site fraction of the offset signal increased while the site fraction of the low frequency decreased, and correspondingly the spectrum became flatter. Similar to LaPd$_3$, this trend should be from the reorientation of the EFG by fast jumping of point defects near ^{111}In/Cd probe at high temperatures.

CePd$_3$ samples were made for both boundaries A and B, including one CePd$_3$(A) sample and four CePd$_3$(B) samples. The adjacent phases of CePd$_3$ are Ce$_3$Pd$_5$ and CePd$_7$ (Fig. 21). The sample CePd$_3$(A) had nominal composition range of 15.0-20.4 at % Ce. There were only two signals in sample CePd$_3$(A), i.e. the dominant signal here was a mean frequency signal, $\overline{\omega_1} = 29.4\ Mrad/s$ with site fraction 93(3) at % at RT (Fig. 23). This signal was due to the ^{111}In/Cd at Ce site affected by the EFG from Pd_{Ce} or V_{ce} at the SNN Ce site. The minority signal was the offset signal with site fraction 12(1) at % at RT, which is from the ^{111}In/Cd at Ce-site interacting with the EFG from Pd atoms at the Nearest Neighbor (NN) sites. As temperature increased, the site fraction of the minority signal had small increase to 18.3(9) at % at 873K, i.e. the site preference of CePd$_3$(A) phase was approximately independent of temperature.

Three of four CePd$_3$(B) samples showed cubic signals, and their nominal composition ranges are (B1) 24.3-29.1 at % Ce, (B2) 27.9-32.9 at % Ce and (B3) 30.5-36.5 at % Ce. They had similar spectra and the right part of Fig. 22 is taken from sample CePd$_3$(B3) as an example. Similar to CePd3(A), spectra of CePd$_3$(B) had only cubic signals, the offset signal as the dominant signal and the low frequency signal as the minority signal. However, the offset signal had larger site fraction than CePd3(A), 45(1) at % at RT. The spectrum of CePd$_3$(B) did not change with the increase of temperature (Fig. 21), which shows independence of site preference of CePd$_3$(B) on temperature.

Note that the peaks of CePd$_3$(B) are broader width than CePd$_3$(A) at half maximum amplitude. This broader peak behavior was related to the width of CePd$_3$ phase in the phase diagram (Fig. 21). Specifically, CePd$_3$(B) is close to the minimum Pd-composition while CePd$_3$(A) is around maximum Pd-composition. In this case, these two phases have different concentrations of defects and thus show different widths in their spectra.

However, there was one CePd$_3$(B) sample showing high frequency signals. As temperatures increased, the ratio f(Ce)/f(Pd) decreased (Fig. 23), and the fitted transfer enthalpy was 0.7(2) eV. Since it is well-known that In/Cd would have equal properties at both Ce-site and Pd-site at extremely high temperatures, the results shows that the enthalpy of In/Cd at Ce-site is lower than Pd-site at low temperatures.

La-Pd Crystal Structure Data

Phase	Composition, at.% Pd	Pearson symbol	Space group	Struktur-bericht designation	Prototype
(γLa)................	0	$cI2$	$Im\bar{3}m$	$A2$	W
(βLa)................	0	$cF4$	$Fm\bar{3}m$	$A1$	Cu
(αLa)................	0	$hP4$	$P6_3/mmc$	$A3'$	αLa
La$_7$Pd$_3$(a)	30	$hP20$	$P6_3mc$	$D10_2$	Fe$_3$Th$_7$
LaPd(b)...........	50	$oC8$	$Cmcm$	B_f	CrB
La$_3$Pd$_4$(c)........	57.1	$hR14$	$R\bar{3}$	...	...
LaPd$_3$(d).........	75	$cP4$	$Pm\bar{3}m$	$L1_2$	AuCu$_3$
(Pd)................	100	$cF4$	$Fm\bar{3}m$	$A1$	Cu

(a) From [73Mor]. (b) From [75Pal]. (c) From [74Pal]. (d) From [61Dwi].

Table 3. Crystal structure data of La-Pd system (taken from Ref. [18])
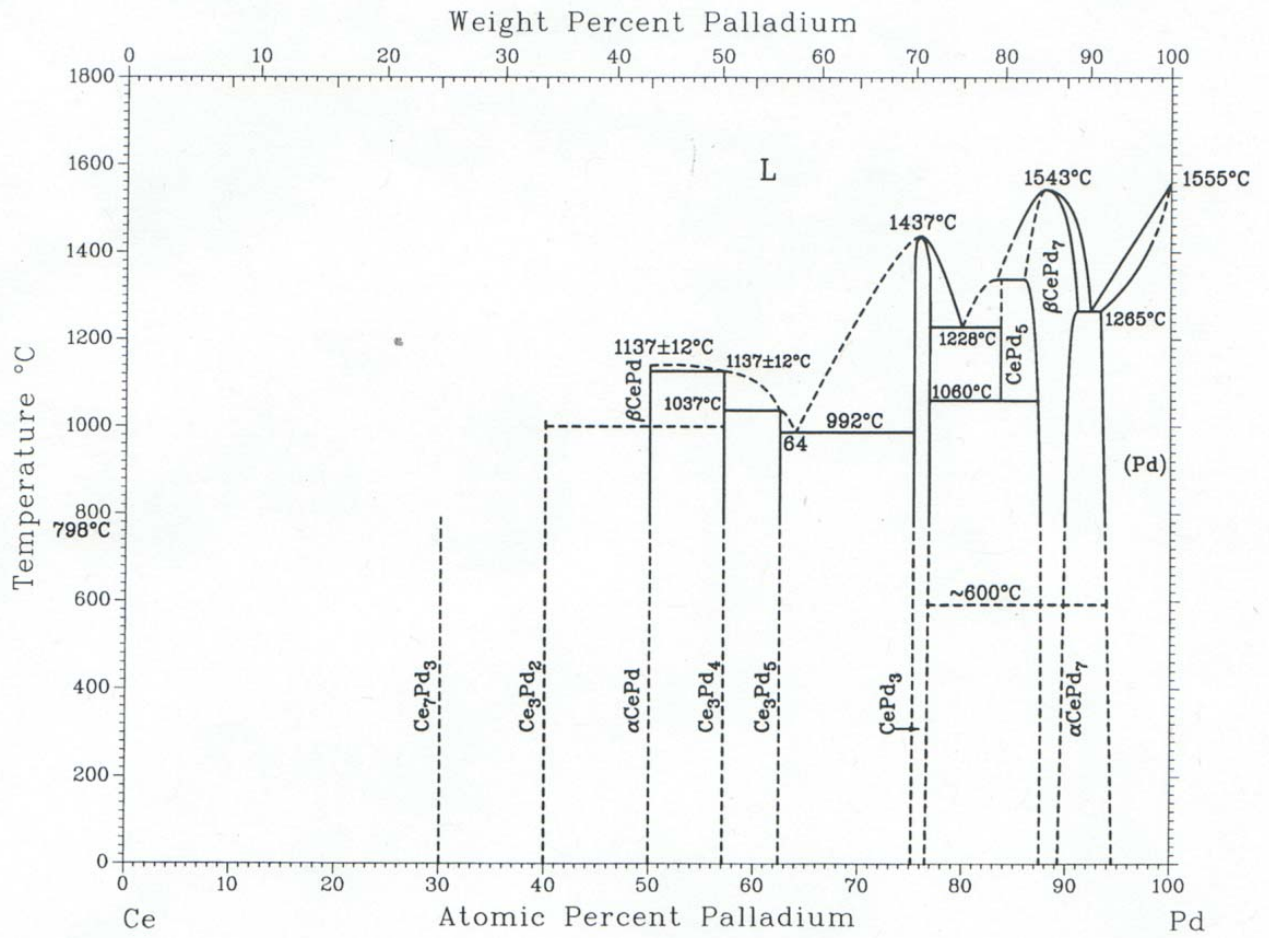
Fig. 21. Phase diagram of Ce-Pd system (taken from Ref. [18])
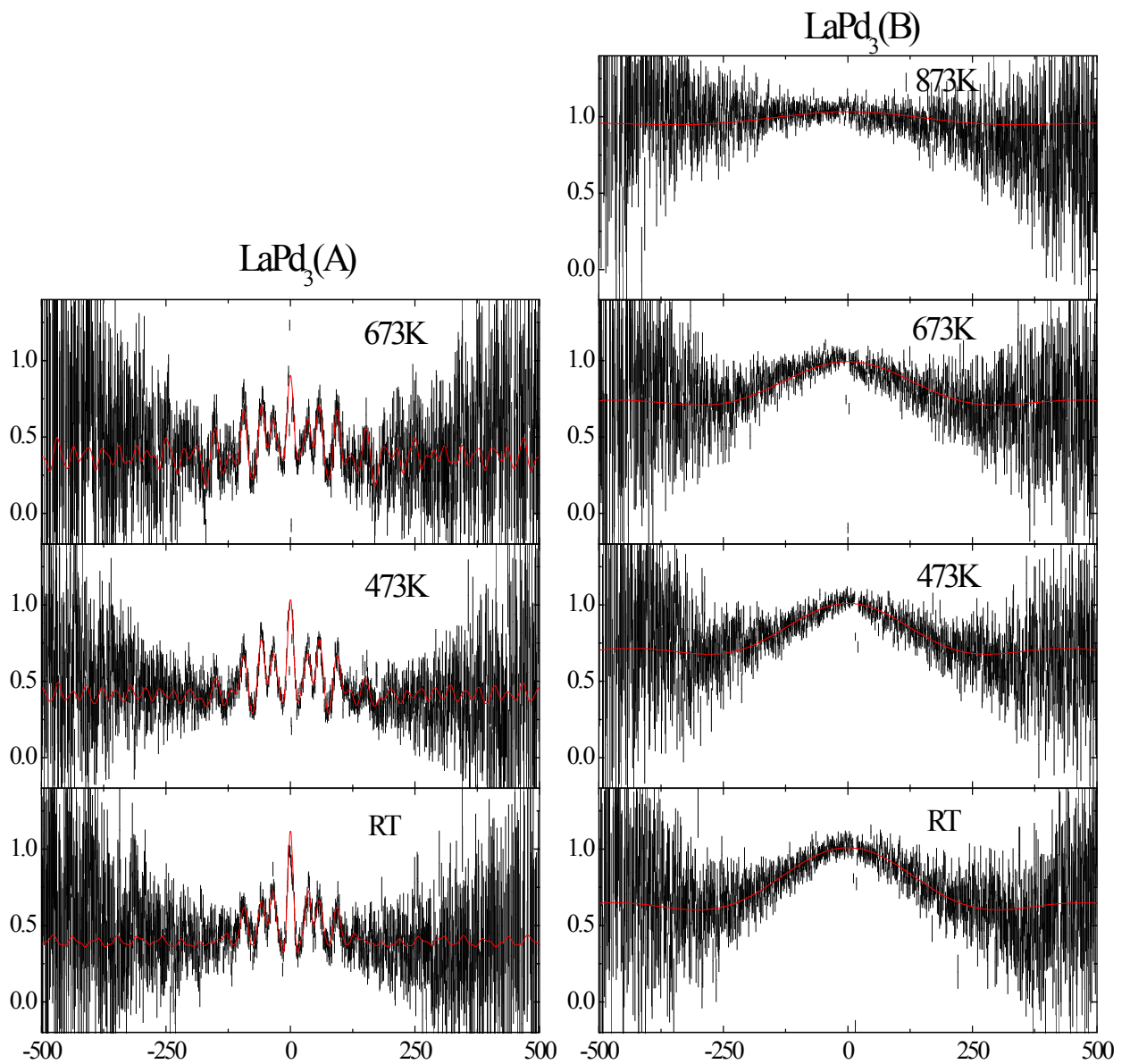
Fig. 22. PAC spectra of LaPd$_3$ at phase boundary compositions A and B. Solid lines are best fits of perturbation functions to Eq. (20).
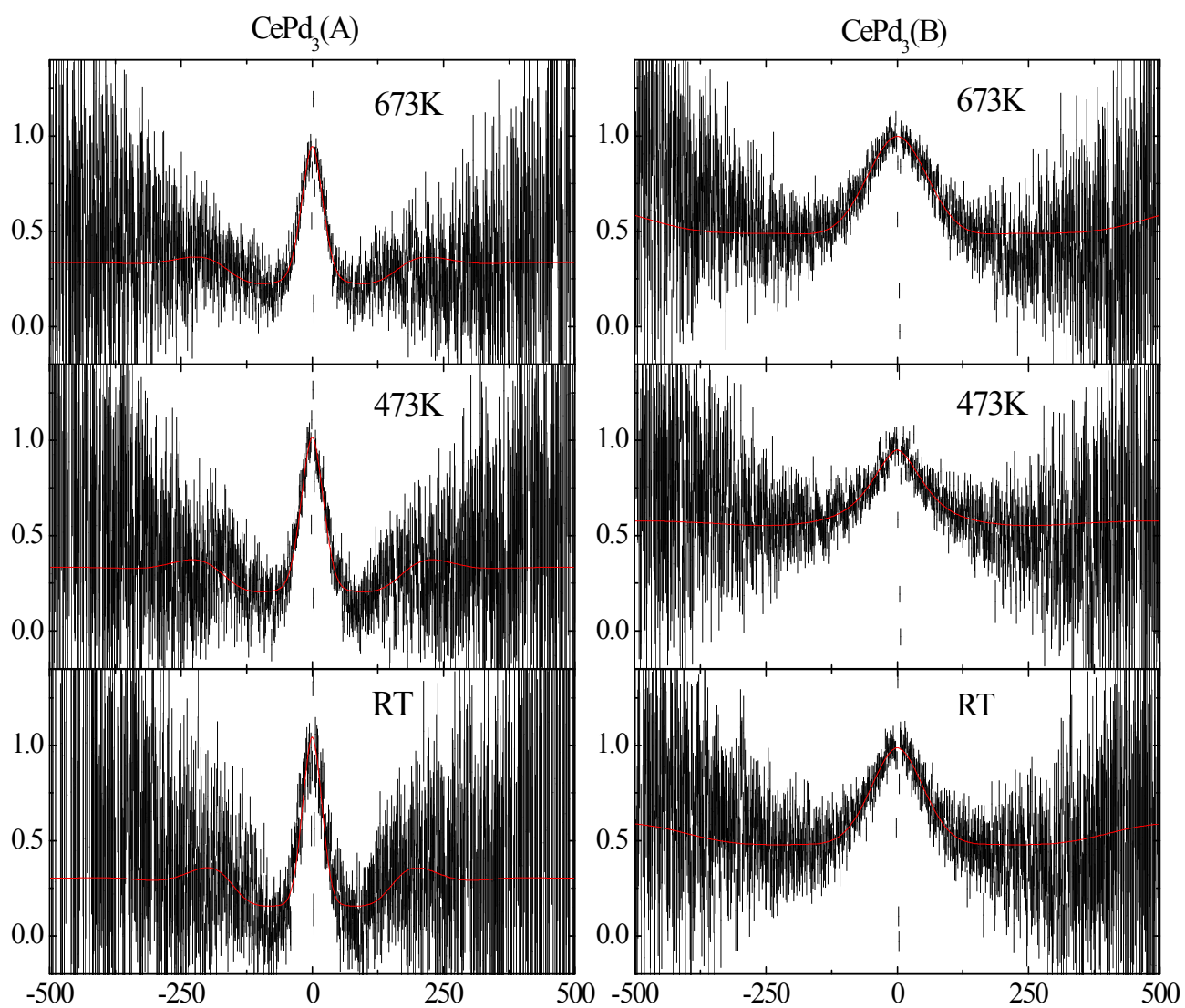
Fig. 23. PAC spectra of CePd$_3$ at opposing phase boundaries A and B. Solid lines are the best fits of perturbation function to Eq. (20).
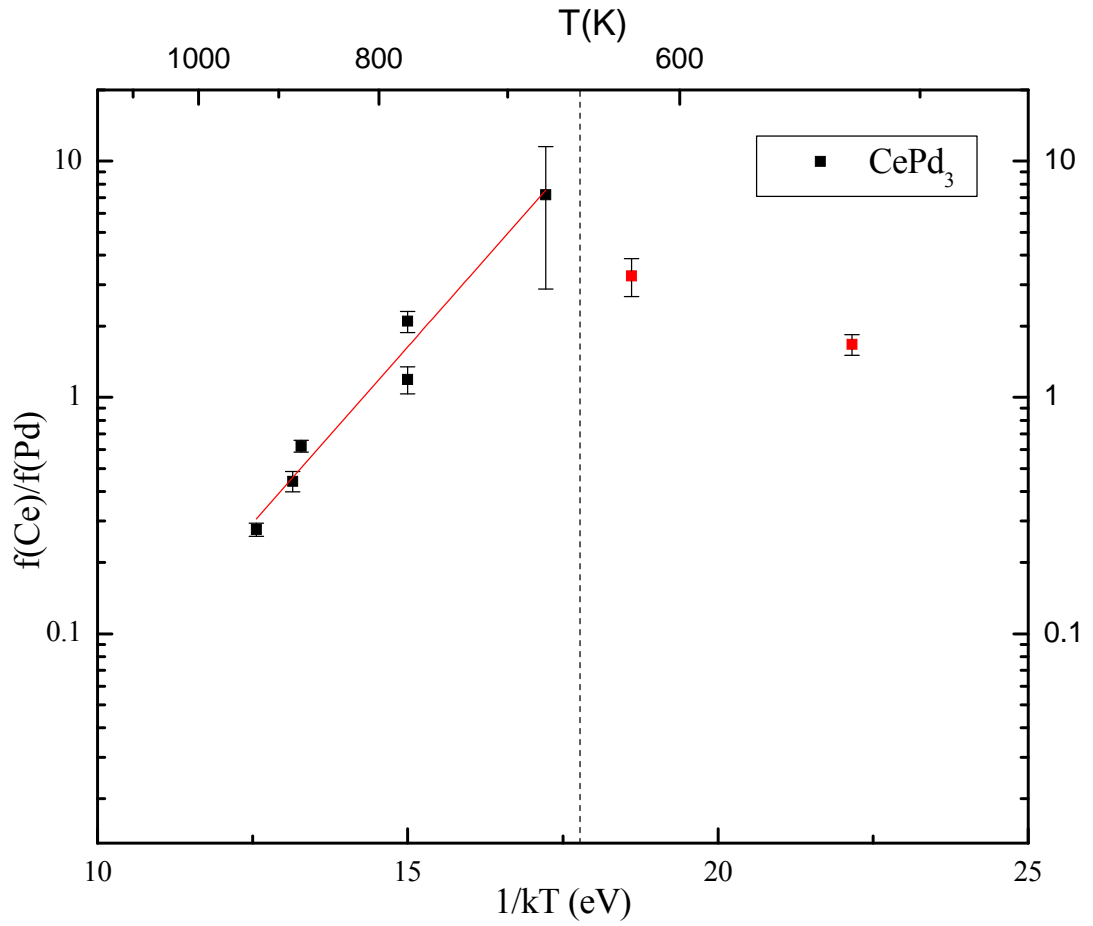
Fig. 24. Ratio of site fraction of In/Cd on Ce-site over site fraction of In/Cd on Pd-site, plotted versus inverse temperature. Solid line is best fit to Eq. (26). Dash line separates equilibrium region and non-equilibrium region.

Chapter 5: Discussion

5.1 Site preferences of In solutes

The spectra of rare-earth palladium phases RPd_3 showed interesting site preferences which had not been observed in other $L1_2$ phases. Table 4 summarizes the site preferences of rare earth palladium phases having the $L1_2$ structure. For RPd_3 phases at the boundary A, ^{111}In probe atom always stays on R-site where only low frequency and offset signals can be measured. However, at the boundary B, most of rare-earth palladides (RPd_3, R=from Pr to Lu, and Sc and Y) have high frequency signals ($\omega_1 \approx 110$ Mrad/s) as the majority signals which are attributed to ^{111}In probe atom on Pd site. Specifically, R=Pr, Nd, Sm and Eu have the coexisting site occupations with site fractions from both R-site and Pd-site. Nevertheless, $LaPd_3$(B) and $CePd_3$(B) are the two different phases where In probe atom only goes to rare-earth site even in the Pd site deficiency case.

In table 5 site preferences of different phases are compared, including $L1_2$ phases R=Pr, Nd, Sm and Eu, C15 structure phase $GdAl_2$, and Ga_7Pd_3. One can see that indium solutes have lower enthalpy on R-site for R=Ce, Pr and Nd, while for R=Sm and Eu the enthalpy of Pd-site is lower. The magnitudes of transfer enthalpies are also comparable to those in other phases, e.g. $GdAl_2$, and Ga_7Pd_3. For comparison, Ga_7Pd_3 has two types Ga-sites and ^{111}In switches from the Ga(3)-site to Ga(4)-site with the increase of temperature.

Fig. 25 gives the change of transfer enthalpies on rare-earth elements. The trend is surprisingly close to linear relationship. From R=Ce to R=Eu, the transfer enthalpy Q changes from positive to negative, showing a very smooth transition.

Table 4. Site preferences of rare-earth palladides. 'Pd' represents ^{111}In probe atoms prefers to occupy the Pd site than the rare-earth site, while 'R' means ^{111}In probe atoms only stays on the rare-earth site.

	La	Ce	Pr	Nd	Pm	Sm	Eu
Pd-poor							
R-poor	*						

	Gd	Tb	Dy	Ho	Er	Tm	Yb	Lu	Y	Sc
Pd-poor										
R-poor										

In/Cd goes to Pd-site

In/Cd prefers R-site

No data

In/Cd goes to R-site and new phase

Table 5. Site preferences versus change of temperature for four different phases. Here notations of elements represent sites where ^{111}In probe prefers to go. Corresponding activation enthalpies are also provided.

Phase	Low T	High T	Q[eV]	Ref.
$CePd_3$	R	Pd_3	0.7(1)	This work
$PrPd_3$	R	Pd_3	0.5(1)	This work
$NdPd_3$	R	Pd_3	0.32(9)	This work
$SmPd_3$	Pd_3	R	-0.07(2)	This work
$EuPd_3$	Pd_3	R	-0.14(1)	This work
$GdAl_2$	R	Al_2	0.343(7)	[3]
Ga_7Pd_3	Ga(3)	Ga(4)	0.10(1)	[20]
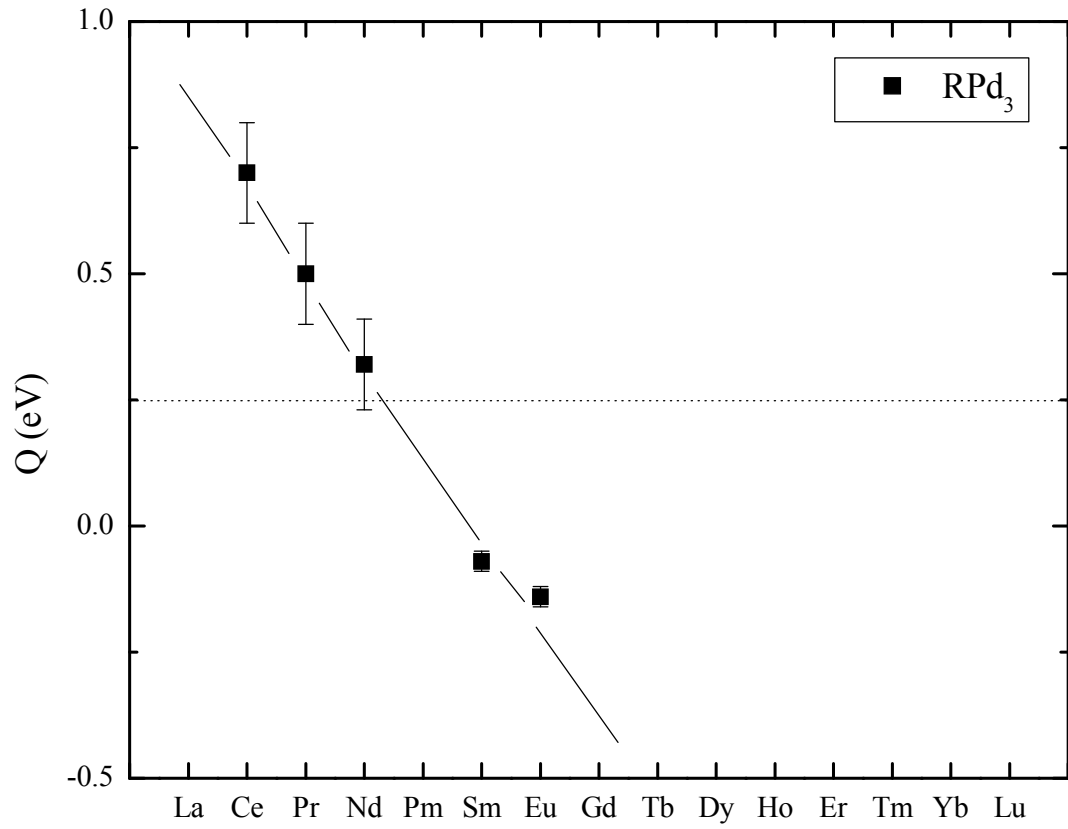
Fig. 25. Transfer enthalpies of rare-earth palladium phases fitted from Eq. (26), plotted versus rare-earth elements. Solid line is given to guide the eyes.

5.2 Quadrupole interaction frequencies of Cd impurities on Pd-sublattice

In Fig. 26, plots about quadrupole interaction frequency ω_1 as a function of temperature are given for rare-earth palladium phases RPd$_3$. All these curves can be fitted by a linear function

$$\omega_1(T) = \omega_1(0°C)(1 + \beta T) \qquad (27)$$

where $\omega_1(0°C)$ is the quadrupole interaction frequency at zero temperature $T = 0°C$, β is the slope of the linear fit regarding the change of frequency with temperature. All the plots for different rare-earth palladium phases can be put together by replotting the ratio of quadrupole interaction frequencies at temperature T over quadrupole interaction frequencies at temperature 0°C, versus change of temperature (see Fig. 27). Values of $\omega_1(0)$ and β for different RPd$_3$ phases are also listed in table 6. One can see that at zero temperature, as the rare-earth R changes from Pr to Lu, the slope β i.e. the change of frequency with temperature is about two times for PrPd$_3$ as the slopes for LuPd$_3$ and YPd$_3$.

Fig. 28(a) further proves that ω_1 has approximately linear dependence on the change of rare-earth R, both at RT and 673K. However, when compare Fig. 28(a) with Fig. 28(b), one can find that in rare-earth palladides, frequency becomes lower if the lattice constant a decreases. The changes of ω_1 at 0℃ and β with lattice parameter are further studied in Fig. 29. The ω_1(0℃) and β both have approximately linear dependences on lattice parameter. This behavior is unique because other L1$_2$ phases at room temperature show an decrease of frequency with the increase of lattice constant (see Fig. 30). Moreover, for rare-earth palladides β increases with the increase of lattice parameter, while slopes β for RIn$_3$ are about constant which is about $2 \times 10^{-4} \, K^{-1}$ (see Ref. [28]). This change of slopes may be due to different thermal expansion coefficients for different RPd$_3$.
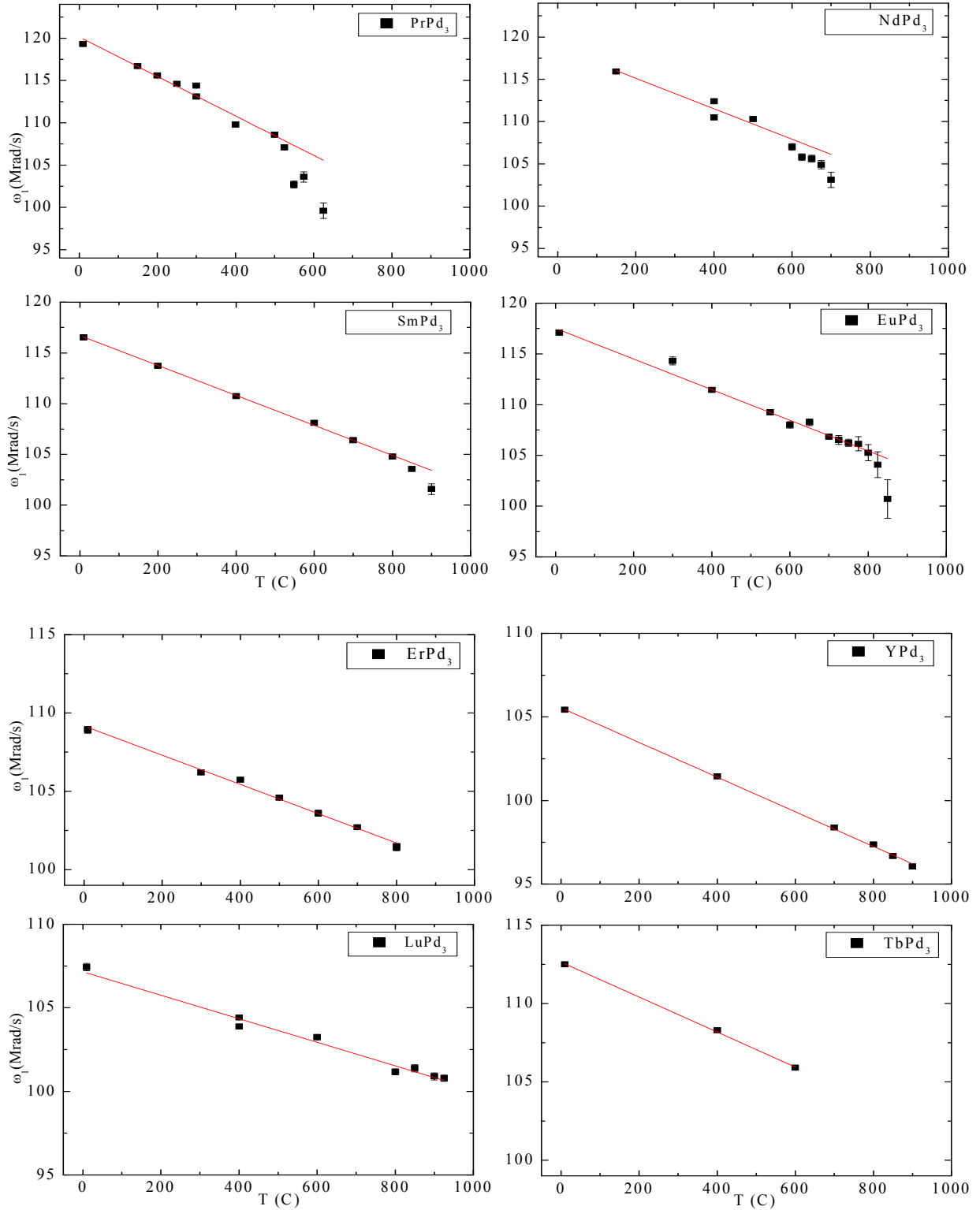
Fig. 26. Quadrupole interaction frequency ω_1 for RPd$_3$ phases, plotted versus absolute temperature, R=Pr, Nd, Sm, Eu, Tb, Er, Lu, Sc and Y.
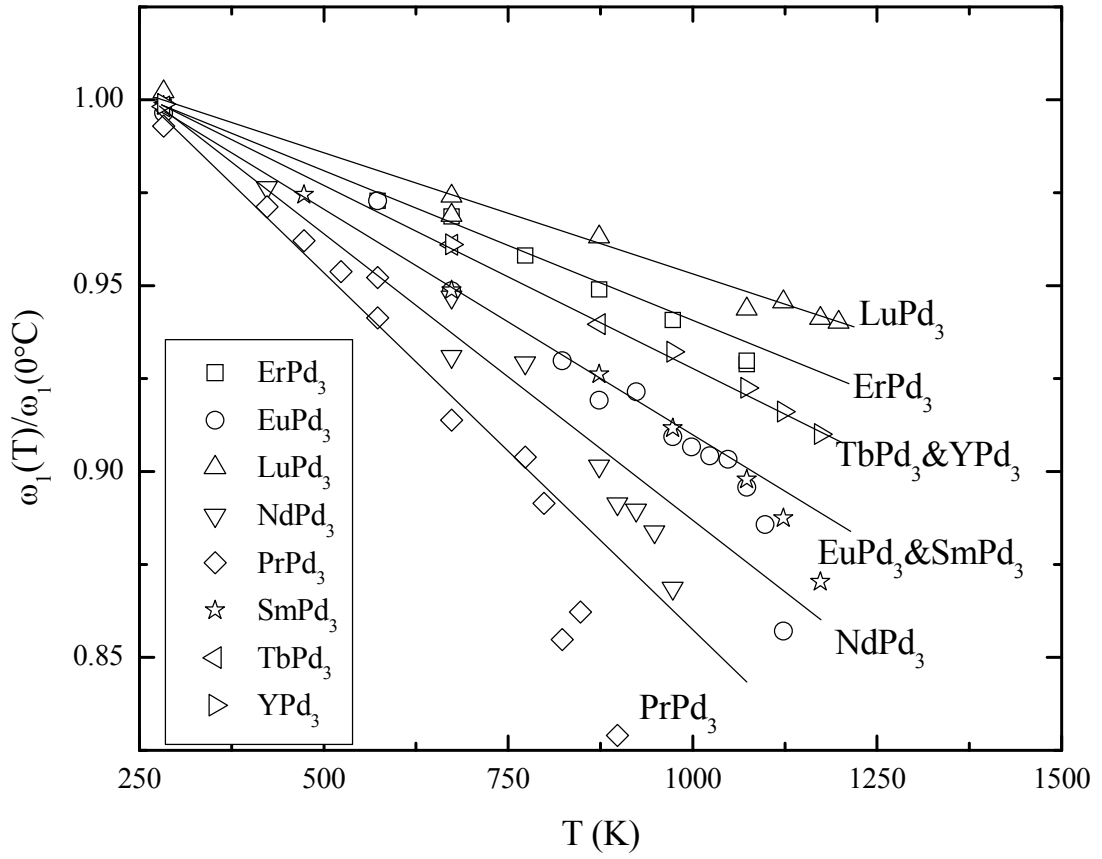
Fig.27. Ratio of quadrupole interaction frequencies at temperature T over temperature 0°C, plotted versus Celsius temperature. Solid lines are fits to Eq. (27).

Table 6. List of $\omega_1(0)$ and β for RPd$_3$ phases, R=Pr, Nd, Sm, Eu, Tb, Er, Lu, Sc and Y.

Phase	$\omega_1(0)$ $(Mrad/s)$	$\beta(K^{-1})$
PrPd$_3$	120.15(8)	1.91(3)
NdPd$_3$	118.7(1)	1.52(3)
SmPd$_3$	116.72(7)	1.268(9)
EuPd$_3$	117.5(2)	1.29(3)
TbPd$_3$	112.7(1)	0.99(2)
ErPd$_3$	109.17(1)	0.852(9)
LuPd$_3$	107.2(1)	0.65(2)
YPd$_3$	105.55(5)	0.982(8)
ScPd$_3$	95(2)	0.9(2)
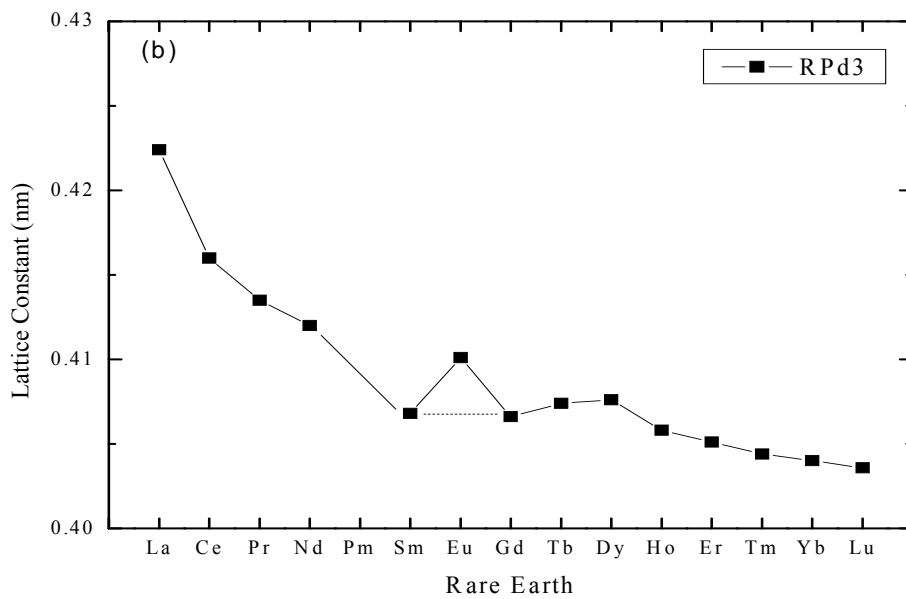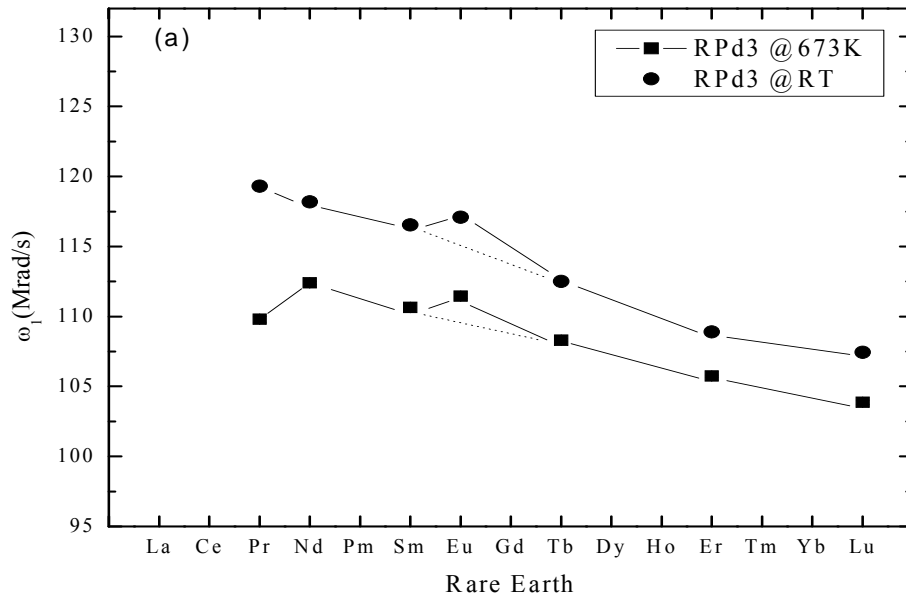
Fig. 28. (a) Experimental quadrupole Frequency ω_1 of ^{111}In solutes at Pd-poorer boundary, plotted versus rare-earth elements at temperatures RT and 673K, lines to guide the eyes; (b) lattice constant for RPd$_3$.
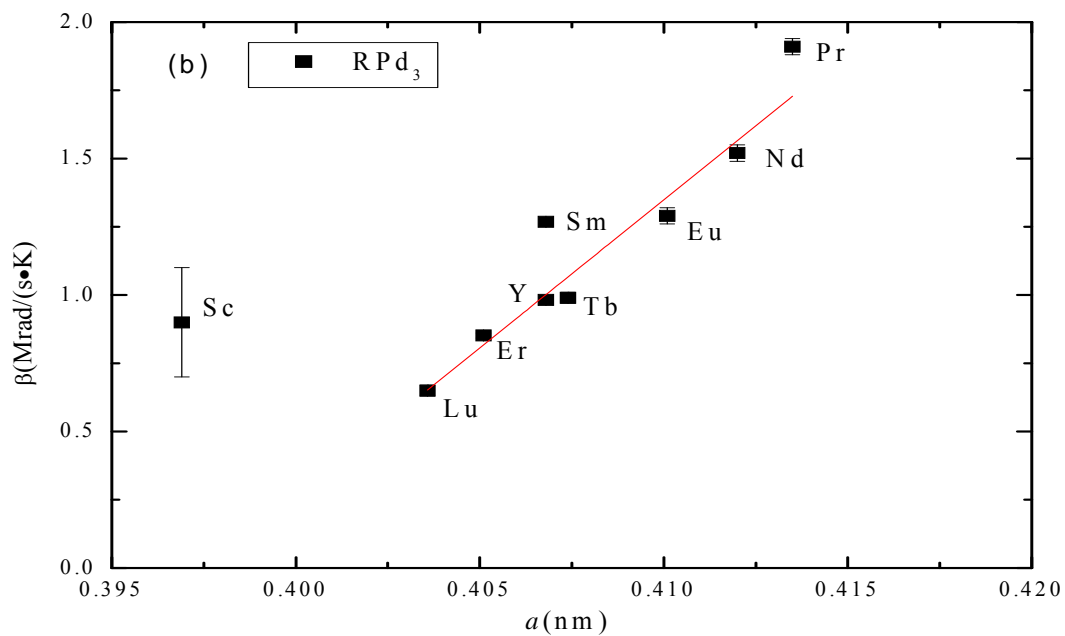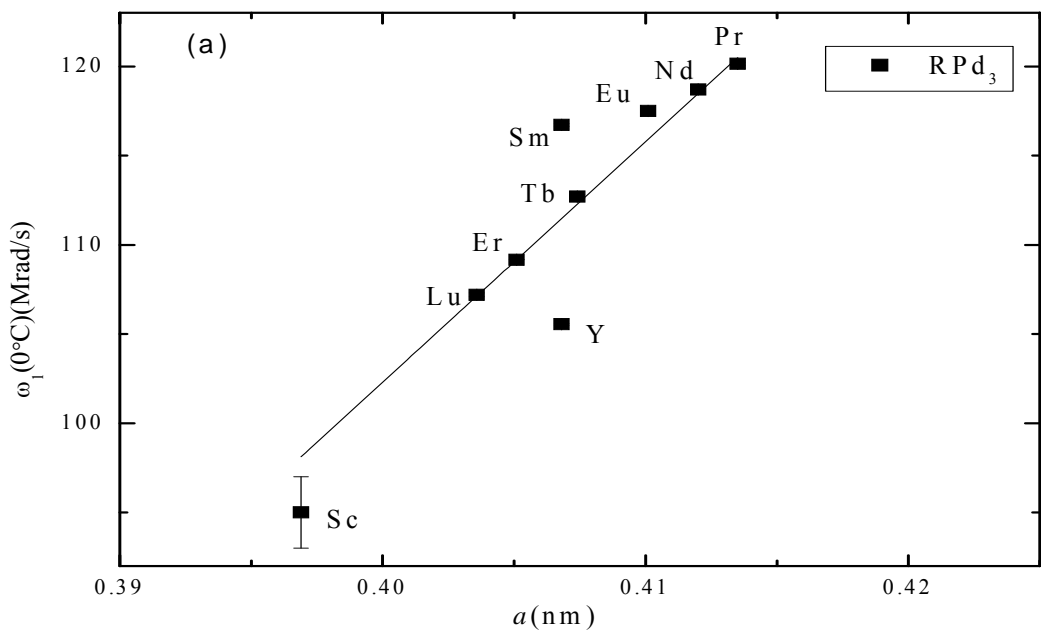
Fig. 29. Quadrupole interaction frequencies ω_1 at 0℃ (a) and slopes β (b) from fits to Eq.(27) for RPd$_3$, plotted versus lattice parameters. Solid lines to guide the eyes.
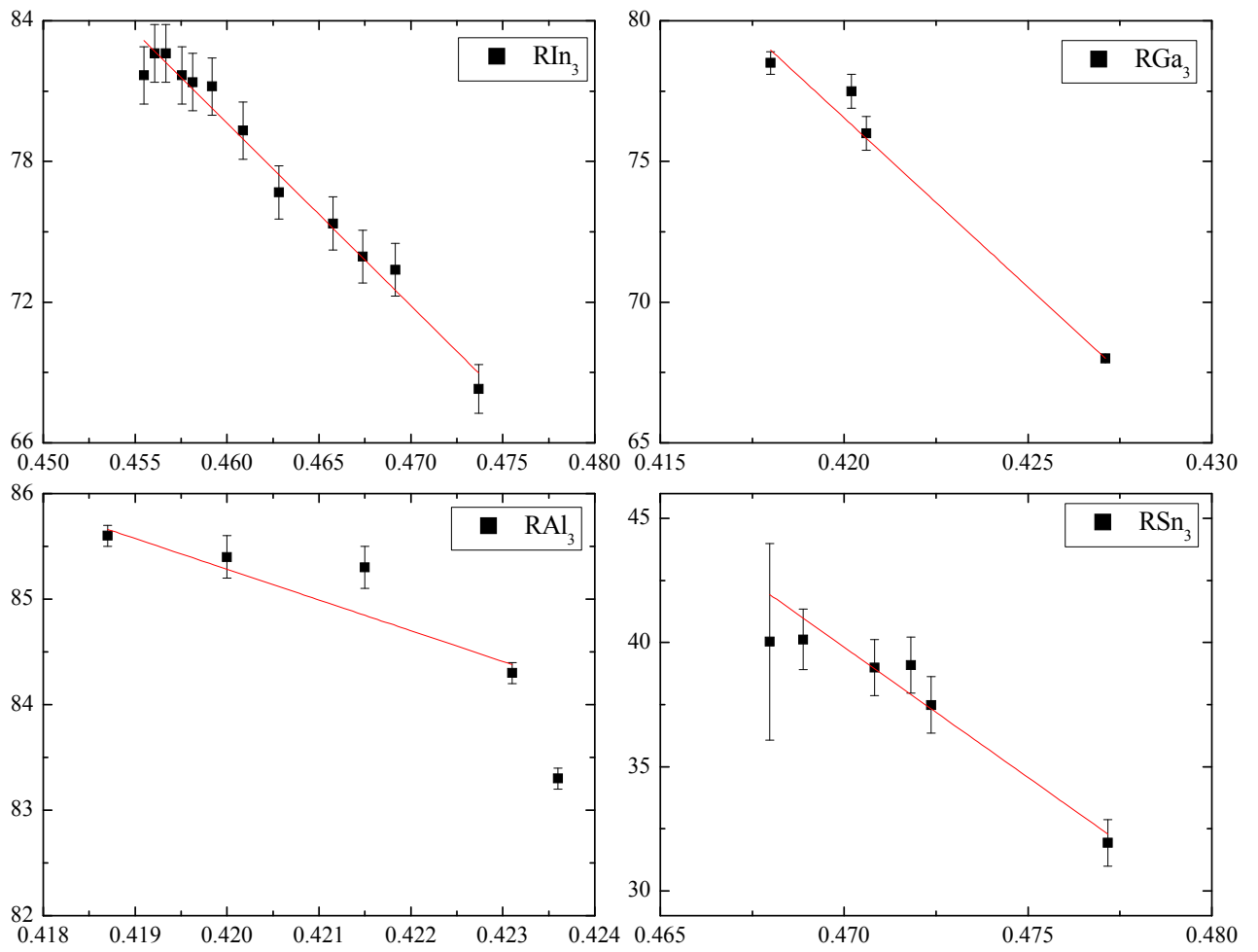
Fig. 30. Quadrupole interaction frequencies at RT for RX$_3$ phases, X=In, Ga, Al and Sn, plotted versus lattice parameters. Solid lines are provided to guide the eyes.

5.3 Comparison of EFG's in RPd$_3$ with EFG's in other L1$_2$ phase systems

In this section, quadrupole interaction frequencies ω_1 and jump frequencies w of ^{111}In probe atoms in six different L1$_2$ phases RX$_3$ are summarized, including X=In, Pd, Ga, Al, Sn and Pb. The dependence of frequency on lattice constant in L1$_2$ phases can be explained by point charge model [21], which states that the EFG of probe atom is inversely proportional to a^3

$$V_{zz} = \alpha \frac{1}{a^3} \tag{29}$$

$$\alpha = (1-k)(1-\gamma_\infty^{X_0})\frac{8.67e}{4\pi\epsilon_0}\Delta Z \tag{30}$$

where k is the electric enhancement factor and in many cases found to be about 3. $\gamma_\infty^{X_0}$ is the so-called sternheimer antishielding factor usually calculated by Hartree-Fock method. ΔZ is the difference between effective charges of A and B in L1$_2$ phase A$_3$B, $\Delta Z = Z_B^{eff} - Z_A^{eff}$, where B is the rare-earth component and A is the transition metal component.

Fig. 31 gives the plots of $\omega_1 a^3$ for RX$_3$ phases. The coefficient α in Eq. (30) is about 8 for RIn$_3$ and RPd$_3$, 6 for RGa$_3$ and RSn$_3$ and 4 for RAl$_3$ and RPb$_3$. The value of $\omega_1 a^3$ is almost constant for different rare-earth elements showing that the data fits fairly well in the point charge model, except the slightly decreasing trend of RPd$_3$. Since α is proportional to ΔZ, the larger the coefficient α, the biggest the effective charge difference. Generally, In and Pd can be put together as group I which has the similar effective number, also for Ga and Al as group II and for Sn and Pb as group III. The group I has the largest effective charge difference, while the group III has the smallest effective charge difference.

$$Effective\ Charge\ Difference: (In \approx Pd) > (Ga \approx Al) > (Sn \approx Pb)$$
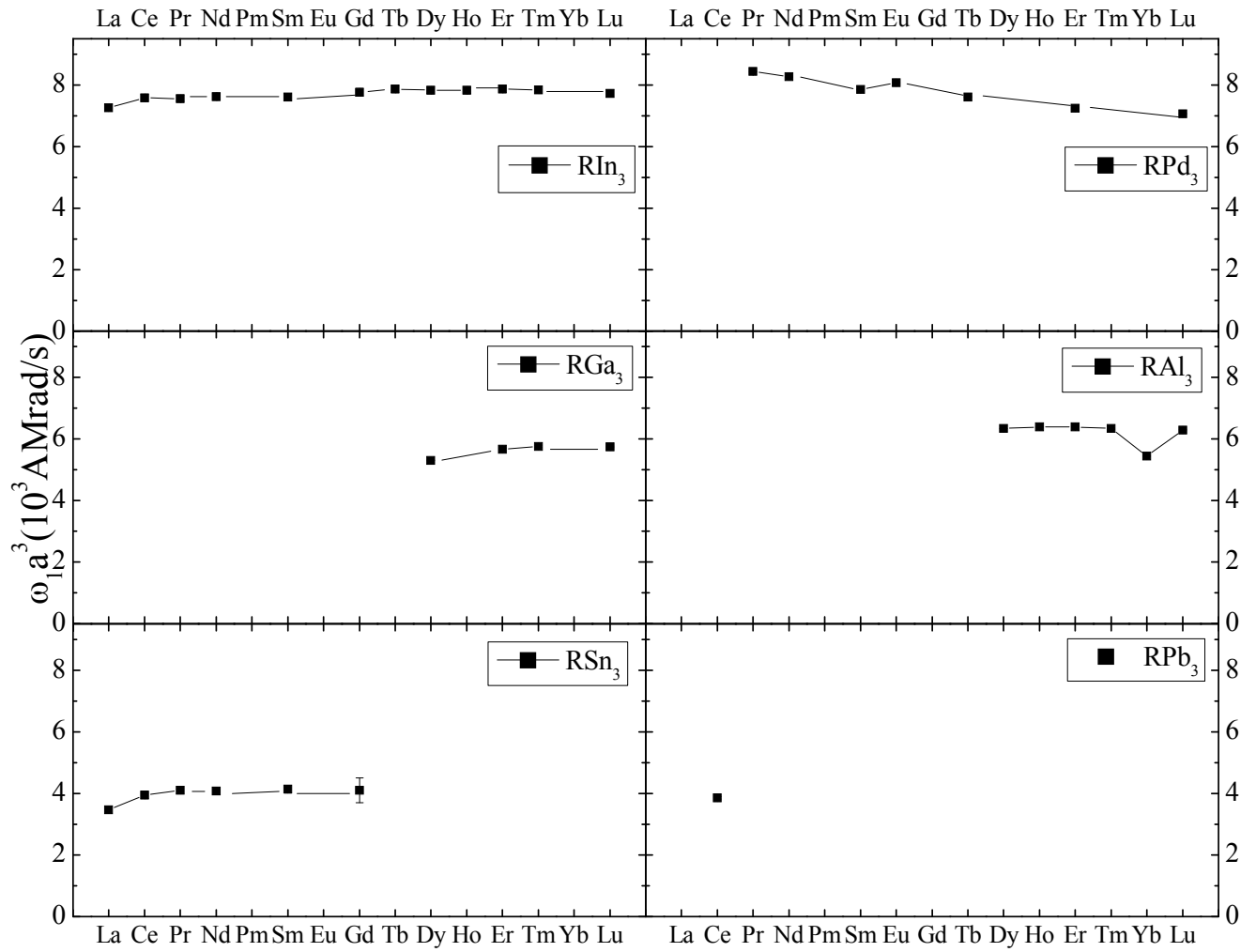
Fig. 31. $\omega_1 a^3$ in unit of $nm - Mrad/s$ for six different L1$_2$ phases at room temperature, plotted versus lanthanide elements. Lines are given to guide the eyes.

5.4 Jump frequencies of Cd impurity on Pd-sublattice

Dynamical relaxations were measured for RPd3, R=Pr, Nd, Sm and Eu at the B boundary. Fig. 32 shows the change of jump frequency with temperature for these four $L1_2$ phases. Generally, dependence of jump frequency on temperature can be fit by

$$w = w_0 \exp\left(-\frac{Q}{kT}\right) \tag{28}$$

where w_0 is the prefactor which does not depend on temperature, Q is the activation enthalpy regarding the switch of ^{111}In probe atom between Pd sites, and k is the Boltzmann constant, $8.6 \times 10^{-5} J/K$.

At fixed temperature, PrPd3 has the highest jump frequency, followed by NdPd3 and EuPd3, and the jump frequency of SmPd3 is the smallest, and their activation enthalpies Q are 0.77(18)eV, 1.10(28)eV, 1.14(11)eV and 2.19(13)eV, for R=Pr, Nd, Sm and Eu respectively. The order of activation enthalpies of these phases agrees very well with the order of their lattice constants, which shows that the smallest lattice constant would cause the highest activation enthalpy.

For other RPd3(B) phases (R=from Gd to Lu), dynamical relaxation cannot be seen possibly because of two reasons: 1. the activation enthalpy between Pd sites is so high that jumping of Cd impurity is prohibited even at very high temperatures; 2. The jumping of Cd impurity cannot be measured by our PAC equipments since only three filaments were used to heat the sample while temperatures higher than 1200K cannot be achieved.

Table 7. The Prefactor and activation enthalpy in Eq. (28) for the four $L1_2$ phases RPd3.

Phases	Q[eV]	w_0[THz]	Lattice Parameter [nm]
CePd3	0.20(3)	2.4(8) $\times 10^{-4}$	0.416
PrPd3	0.77(18)	0.4(11)	0.4135
NdPd3	1.10(28)	6(21)	0.412
EuPd3	1.14(11)	3(3)	0.4101
SmPd3	2.19(13)	$3(4) \times 10^{3}$	0.4068
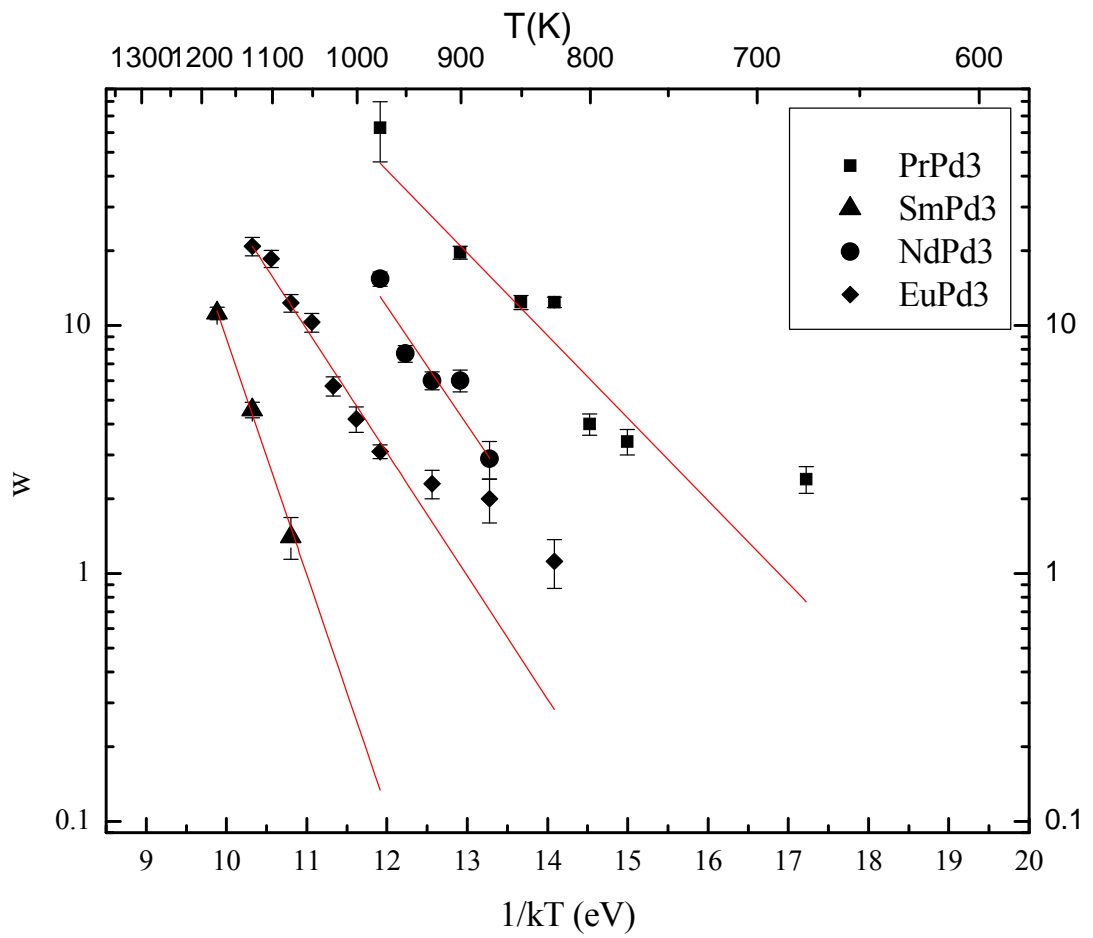
Fig. 32. Jump frequencies for PrPd$_3$, SmPd$_3$, NdPd$_3$ and EuPd$_3$, plotted versus inverse temperature. Solid lines are best fits to Eq. (28).

5.5 Comparison of jump frequencies of Cd impurity for different L1$_2$ phases

Fig. 33 summarizes jump frequencies w of rare-earth L1$_2$ phases people have found (Data can be found in Table 8). Generally, In-site and Al-site have approximately the same activation enthalpies. Taken a further step, at the same temperature, jump frequencies of Cd impurity on In-site is lower than Pd-site and Ga-site, and higher than Sn-site and Pb-site. In conclusion, the activation enthalpies of Pd-site and Ga-site are the highest, while Sn-site and Pb-site have the smallest activation enthalpies.

$$Activation\ Enthalpy\ on\ X\ site: (Pd, Ga) > (In, Al) > (Sn, Pb)$$

In Fig. 34 plots regarding the change of activation enthalpy with lattice constant for the six different L1$_2$ phases are given. One can find that for RIn$_3$ and RPd$_3$, activation enthalpy is approximately a linearly increasing function with the decrease of lattice constant, while for RGa$_3$ and RAl$_3$, activation enthalpy is almost constant with the change of lattice constant. The dependence of RSn$_3$ and RPb$_3$ on lattice constant is still unknown since not much data can be found.

$$Activation\ Enthalpy\ with\ decrease\ of\ lattice\ constant:$$

$$(In, Pd)linear\ increase; (Ga, Al)\ unknown; (Sn, Pb)unknown.$$
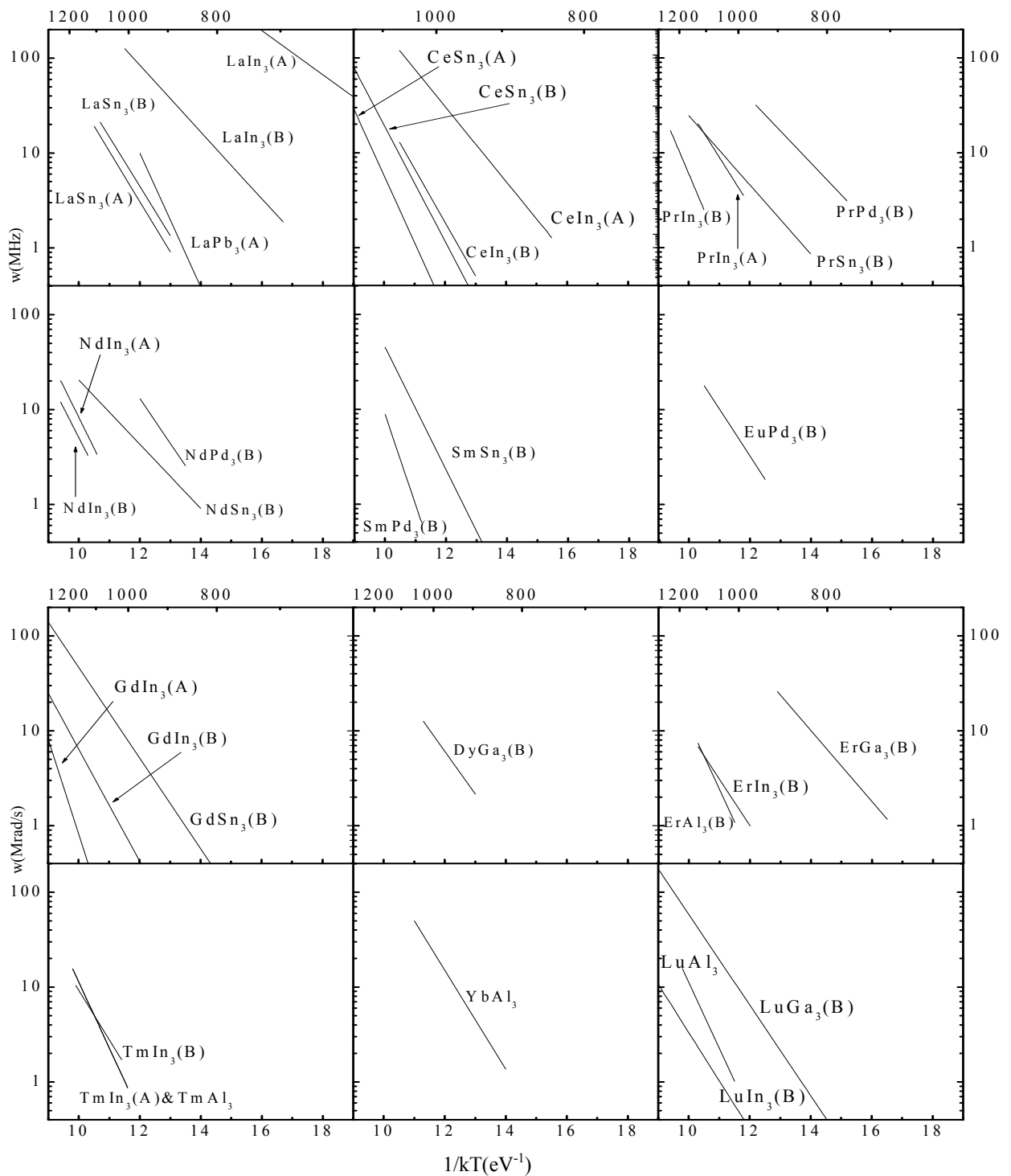
Fig. 33. Jump frequencies of different L1$_2$ phases A$_3$B, plotted versus the inverse temperature. The graphs are arranged in the order of the lanthanide series from upper left to lower right, B=rare-earth.
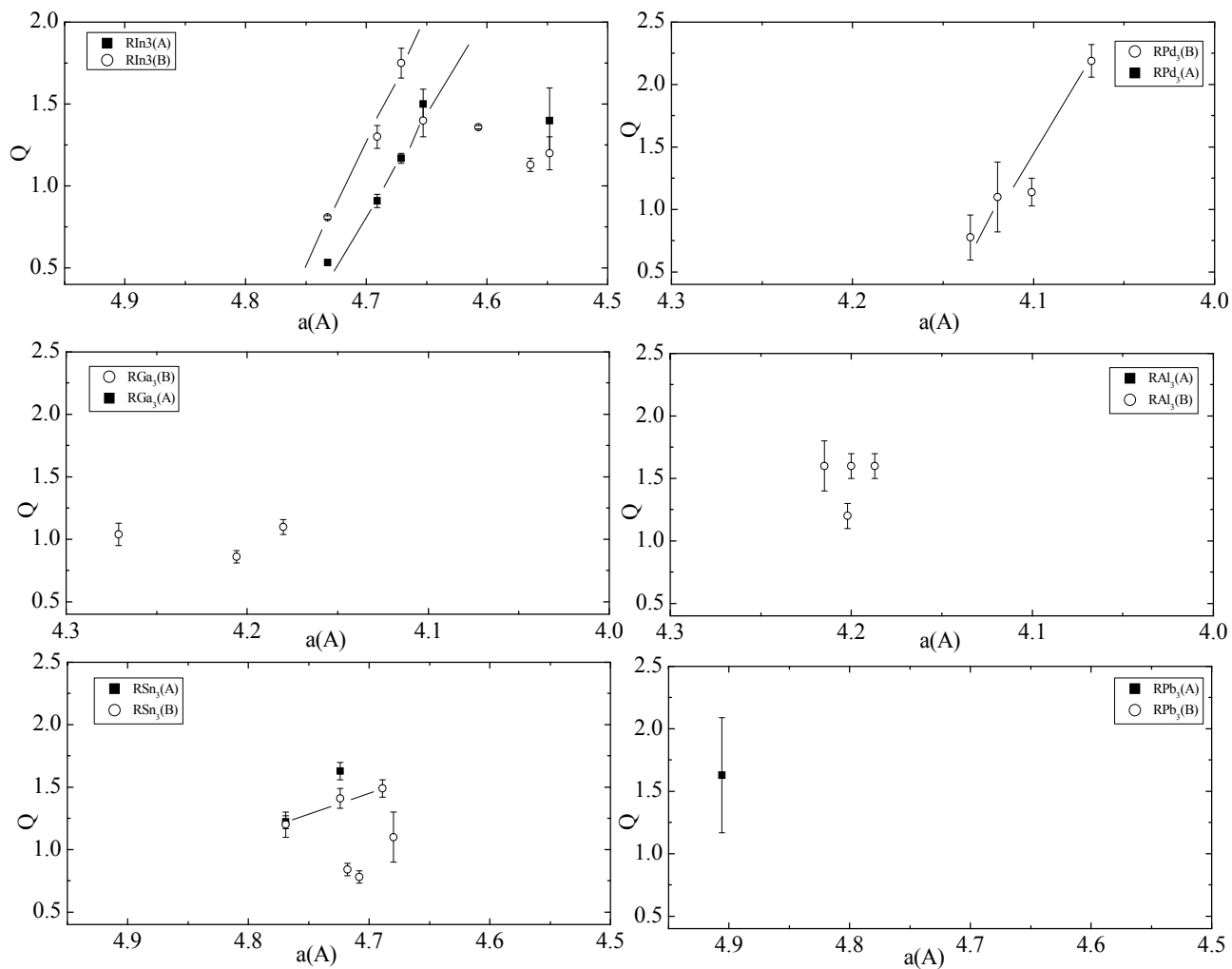
Fig. 34. Jump frequency activation enthalpies for different L1$_2$ phases RX$_3$, plotted versus lattice constant. From the upper left to the lower right, X=In, Pd, Ga, Al, Sn and Pb.

Table 8. Prefactors and activation enthalpies in Eq. (28) for jumping of cadmium impurities in six different L1$_2$ phases.

Phases	Q[eV]	w0[THz]	Lattice Parameter [nm]	Ref.
CePd$_3$ (B)	0.20(3)	2.4(8)$\times 10^{-4}$	0.416	This work
PrPd$_3$ (B)	0.77(18)	0.4(11)	0.4135	This work
NdPd$_3$ (B)	1.10(28)	6(21)	0.412	This work
EuPd$_3$ (B)	1.14(11)	3(3)	0.4101	This work
SmPd$_3$ (B)	2.19(13)	3(4)$\times 10^{3}$	0.4068	This work
LaIn$_3$ (A)	0.535(2)	1.02(5)	0.4732	[22]
LaIn$_3$ (B)	0.81(1)	1.4(2)		[22]
CeIn$_3$ (A)	0.91(4)	1.7(+1.2,-0.7)	0.4691	[22]
CeIn$_3$ (B)	1.30(7)	11(+13,-6)		[22]
PrIn$_3$ (A)	1.17(3)	3.5(1.3)	0.4671	[23]
PrIn$_3$ (B)	1.75(9)	240(120)		[23]
NdIn$_3$ (A)	1.50(9)	27(25)	0.4653	[23]
NdIn$_3$ (B)	1.4(1)	10(10)		[23]
GdIn$_3$ (A)	~2.3	~8000	0.4607	[23]
GdIn$_3$ (B)	1.36(1)	5.2(4.5)		[23]
ErIn$_3$ (B)	1.07(7)	0.62(+0.60, -0.31)	0.4564	[22]
TmIn$_3$ (A)	1.4(2)	5(8)	0.4548	[23]
TmIn$_3$ (B)	1.2(1)	1.5(1.5)		[23]
YIn$_3$	1.43(5)	34(+26,-15)	0.4592	[22]
LuIn$_3$ (A)	2.0(3)	4(1)		[24]
LuIn$_3$ (B)	1.17(4)	0.4(2)		[24]

Phases	Q[eV]	w0[THz]	Lattice Parameter [nm]	Ref.
DyGa$_3$ (B)	1.04(9)	1.6(1.7)	0.4271	[22]
ErGa$_3$ (B)	0.86(5)	1.7(1.3)	0.4206	[22]
LuGa$_3$ (B)	1.10(6)	3.5(2.5)	0.4180	[22]
ErAl$_3$ (B)	1.6(2)	106(208)	0.4215	[22]
TmAl$_3$	1.6(1)	100(+100,-50)	0.4200	[25]
YbAl$_3$	1.2(1)	27(+17,-11)	0.4187	[25]
LuAl$_3$	1.6(1)	100(+100,-50)	0.4202	[25]
LaSn$_3$ (A)	1.29(5)	14(9)	0.4769	[23]
LaSn$_3$ (B)	1.09(10)	3(4)		[23]
CeSn$_3$ (A)	1.63(7)	69(51)	0.4724	[26]
CeSn$_3$ (B)	1.41(8)	26(245)		[26]
PrSn$_3$ (B)	0.84(5)	0.11(6)	0.4718	[26]
NdSn$_3$ (B)	0.78(7)	0.05(4)	0.4708	[26]
SmSn$_3$ (B)	1.49(7)	134(99)	0.4689	[26]
GdSn$_3$ (B)	1.1(2)	2.8(5)	0.4680	[26]
LaPb$_3$ (A)	1.6(5)	$3(19)\times 10^3$		This work
LaPb$_3$ (B)				
CePb$_3$ (A)			0.4875	
CePb$_3$ (B)				

Chapter 6: Summary

Site preferences of indium solutes in rare-earth palladium phases were studied and compared with other phases, e.g. $GdAl_2$ and Ga_7Pd_3. Indium solutes only occupy R-sites for all RPd_3 at the A boundary and for light rare-earth palladides at the B boundary. For intermediate weight and heavy weight rare-earth palladides at the B boundary indium solutes prefer to go to Pd-sites. Interesting changes of site occupations of indium solutes with temperature can be seen for R=Ce, Pr, Nd, Sm and Eu. Specifically, as temperature increases, an indium tracer prefers to switch from R-site to Pd-site for R=Ce, Pr and Nd, and from Pd-site to R-site for R=Sm and Eu.

Quadrupole interaction frequencies of cadmium tracer atoms on Pd sites were measured for RPd_3 at the B boundary. For each RPd_3 phase, quadrupole interaction frequency was found to have linear dependence on temperature, and decrease with the increase of temperature. Throughout the whole rare-earth series, quadrupole interaction frequency also decreases as the atomic number of rare-earth atom increases, or as the lattice constant decreases, and this trend can be regarded as linear dependence approximately. Quadrupole interaction frequencies of six $L1_2$ phases RX_3 (X=In, Pd, Ga, Al, Sn and Pb) were described by the point charge model, and the corresponding effective charge number were determined.

Jump frequencies of cadmium tracer nuclides between Pd-sites were fitted for RPd_3 at the B boundary, and activation enthalpies can only be determined for R=Pr, Nd, Sm and Eu. Activation enthalpies of heavy weight rare-earth palladium phases are too high that dynamical relaxation cannot be seen. It was found that the order of activation enthalpies agrees well with the inverse order of lattice constants, i.e. smaller lattice constant caused higher activation enthalpy. Activation enthalpies of six $L1_2$ phases RX_3 (X=In, Pd, Ga, Al, Sn and Pb) were also summarized and compared for different R atoms and X atoms.

BIBLIOGRAPHY

[1] P. Chartier et al., J. Appl. Phys. 75, 3842 (1994)

[2] Y. L. Hao et al., Intermetallics 8, 633 (2000)

[3] M. O. Zacate, and G. S. Collins, Phys. Rev. B 69, 174202 (2004)

[4] M. O. Zacate, A. Favrot, and G. S. Collins, Phys. Rev. L 92, 225901 (2004)

[5] G. S. Collins, X. Jiang, J. P. Bevington, and F. Selim, Phys. Rev. L 102, 155901 (2009)

[6] D. R. Hamilton, Phys. Rev. 58, 122 (1940)

[7] E. L. Brady and M. Deutsch, Phys. Rev. 72, 870 (1947)

[8] Nuclear Condensed Matter Physics-Nuclear Methods and Applications, G. Schatz, A. Weidinger and J. A. Gardner

[9] Gary S. Collins, Steven L. Shropshire and Jianwen Fan, Hyperfine Interaction 62, 1-34 (1990).

[10] F. Pleiter, Hyperfine Interact 5, 109 (1977)

[11] Frauenfelder and Steffen, 1965

[12] Matthias et al., 1962

[13] A. Baudry, and P. Boyer, Hyperfine Interaction 35, 803 (1987)

[14] C. Zener, Acta Crystallogr. 3, 346 (1950)

[15] S. Maeda, K. Tanaka, and M. Koiwa, Defect Diffus. Forum 95-98, 855 (1993)

[16] Nobuaki Kurita and Masahiro Koiwa, Intermetallics 10, 735 (2002)

[17] T. Ito, S. Ishioka, and M. Koiwa, Philos. Mag. A 62, 499 (1990)

[18] Phase diagram

[19] Phase diagram supplement

[20] Tyler Park et al., Hyperfine Interaction 199, 397-402 (2011)

[21] G. P. Schwartz, and D. A. Shirley, Hyperfine Interaction 3, 67-76 (1997)

[22] G. S. Collins, A. Favrot, L. Kang, E. R. Nieuwenhuis, D. Solodovnikov, J. Wang, and M. O. Zacate, Hyperfine Interactions 159, 1 (2005)

[23] X. Jiang, M. O. Zacate, and G. S. Collins, Defect and Diffusion Forum 289, 725 (2009)

[24] John. P. Bevington, PhD thesis, Washington State University.

[25] M. Forker, and P. de la Presa, Phys. Rev. B 76, 115111 (2007).

[26] M. Lockwood Harberts, B. Norman, R. Newhouse, and G. S. Collins, Defect and Diffusion Forum 311, 159 (2011)

[27] Y. T. Ning et al., Journal of the Less Common Metals, 147, 167-173 (1989)

[28] Gary S. Collins, Aurelie Favrot, Li Kang, Egbert R. Nieuwenhuis, Denys Solodovnikov, Jipeng Wang and Matthew O. Zacate, Hyperfine Interaction 159, 1-8 (2005)

Addendum

This addendum to the thesis of Qiaoming Wang (MS, Physics, May 2012) was prepared by Gary S. Collins with assistance of Randal Newhouse.

1. <u>Corrected analysis of site-fraction ratios observed for NdPd$_3$</u>.   The fit shown in Fig. 14 is erroneous. A revised fit, including one datum omitted from fitting in Fig. 14 is given below. Data below 800K were considered to be quenched-in (out of equilibrium) and were excluded from the fit.

Fig. A1.   *Refit of site fraction ratios observed for NdPd$_3$, including one more datum at higher temperature, but omitting three data at lower temperatures that are believed to not be on samples in thermal equilibrium. Replaces Fig. 14 in the thesis.*

2. <u>Corrected analysis of site-fraction ratios observed for SmPd$_3$</u>.   The fit shown in Fig. 17 omitted a datum point. A revised fit, including the datum is given below.
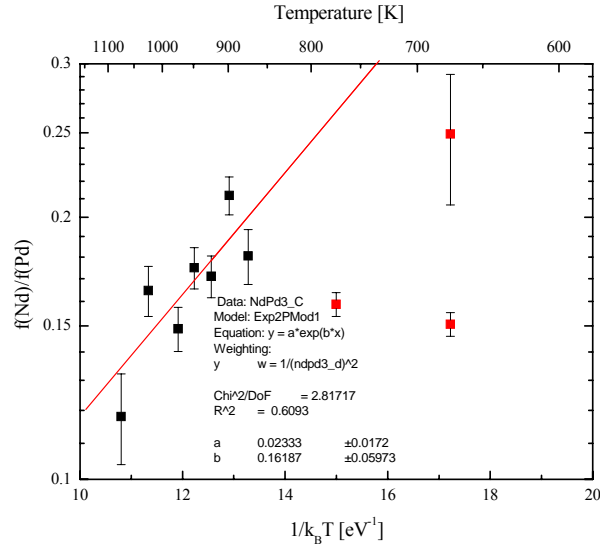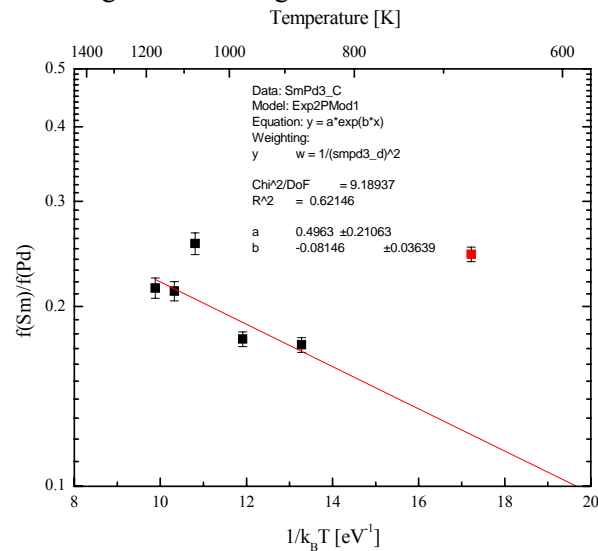

Fig. A2.   *Refit of site fraction ratios observed for SmPd$_3$, including one more datum at higher temperature, and omitting one datum at lower temperatures that is not believed to have been on a sample in thermal equilibrium. Replaces Fig. 17 in the thesis.*

3. Corrected table of activation enthalpies for site preferences of In probe atoms in RPd$_3$ phases obtained from fits of site fraction ratios as a function of temperature. The way in which the site preference data were fitted was not made explicit in the thesis. For consistency, we define as the relevant site-fraction ratio the ratio of site fractions of In-probes on R and Pd sites, f_R / f_{Pd}, and assume it is thermally activated according to

$$\frac{f_R}{f_{Pd}} = A\exp(-Q/k_B T), \tag{A1}$$

in which Q is the site-preference activation enthalpy and A is a prefactor. Data sets shown in Figs. 24, 11(a), A1, A2, and 19 were fitted using Eq. A1, yielding the following table intended to *replace* Table 5 in the thesis. The new table includes revised values for Q, signs for Q consistent with eq. A1, and prefactors A. Also included are separate fits for top and bottom data groups shown for EuPd$_3$ in Fig. 19.

Table A1. Fits of site fraction ratios f_R / f_{Pd} as a function of temperature to Eq. A1 for five RPd$_3$ phases. For GdAl$_2$, f_{Gd} / f_{Al}. For Ga$_7$Pd$_3$, with two inequivalent Ga-sites, the ratio is defined as f(Ga3)/f(Ga4).

Phase	Q [eV]	A	# data points	χ^2	
CePd$_3$	-0.69(10)	0.00006(7)	6	6.608	this work
PrPd$_3$	-0.53(10)	0.00014(19)	5	6.517	"
NdPd$_3$	-0.16(6)	0.023(17)	7	2.817	"
SmPd$_3$	+0.08(4)	0.50(21)	5	9.189	"
EuPd$_3$ (top line)	+0.12(1)	5.1(7)	7	0.518	"
EuPd$_3$ (lower line)	+0.161(9)	6.5(9)	4	3.303	"
EuPd$_3$ average	+0.14(3)	6(2)			"
GdAl$_2$	-0.343(7)	0.001-0.01			[1]
Ga$_7$Pd$_3$	-0.10(1)	0.4(2)	6		[2]

A revised and corrected version of Fig. 25 is given below in Fig. A3.
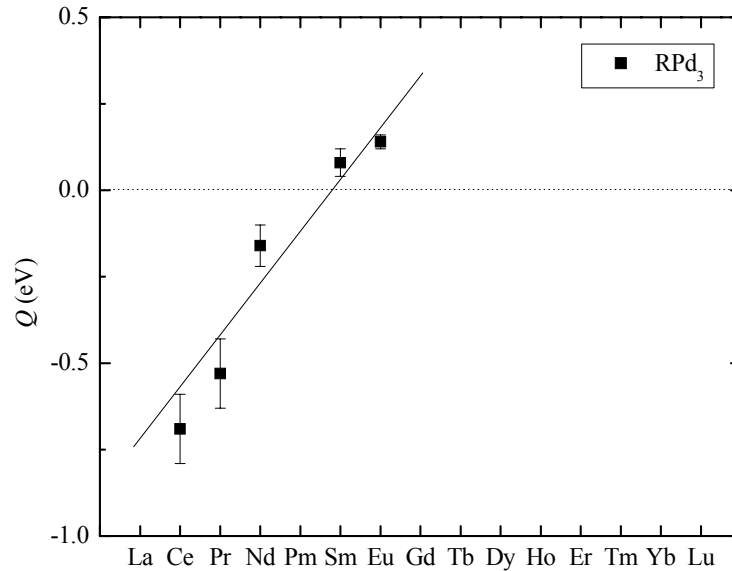
Fig. A3. Dependence of the site-fraction ratio activation enthalpy on atomic number in RPd$_3$ phases.

Negative values of Q for Ce-, Pr- and NdPd$_3$ means that the rare-earth site is preferred by indium solutes at low temperature.

4. <u>Additional comments on jump-frequency activation enthalpies for In/Cd solutes in RPd$_3$ phases</u>.

A revision of Fig. 32 that includes also data for CePd$_3$ is given below. Plotted is the jump frequency w, assumed to be equal to the relaxation frequency λ obtained from a fit of the quadrupole perturbation function to an expression of the form

$$G_2(t) = \exp(-\lambda t) G_2^{static}(t). \tag{A2}$$

Shown in the figure below are Arrhenius plots for $w \equiv \lambda$ for the five RPd$_3$ phases, replacing Fig. 32.
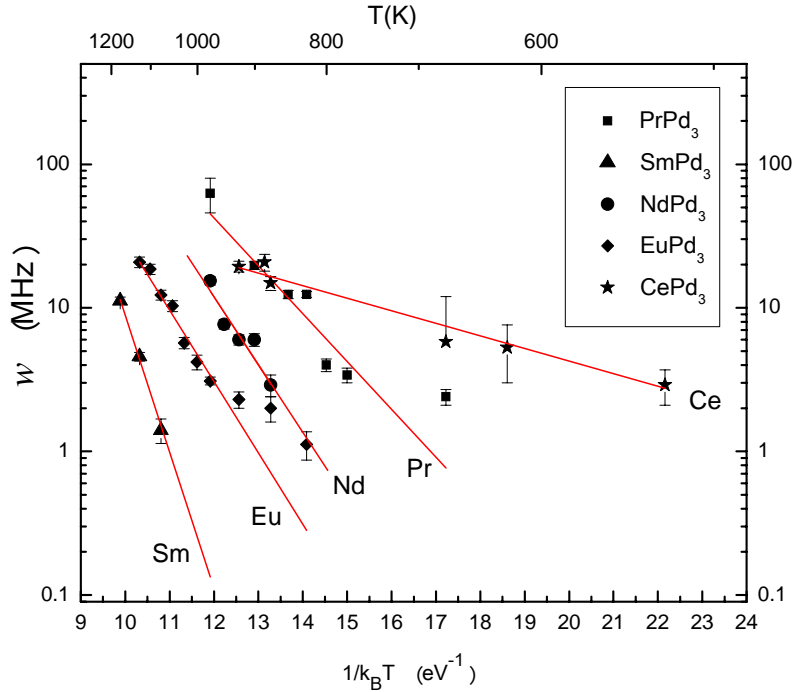
<u>Fig. A4</u>. Arrhenius plots of jump-frequencies of In/Cd probe atoms in five RPd$_3$ phases.

Table 7 gave results for fits of the separate data sets to thermally activated expressions of the form

$$w = w_0 \exp(-Q/k_B T). \tag{A4}$$

Figure A5 shows how Q varies with atomic number.
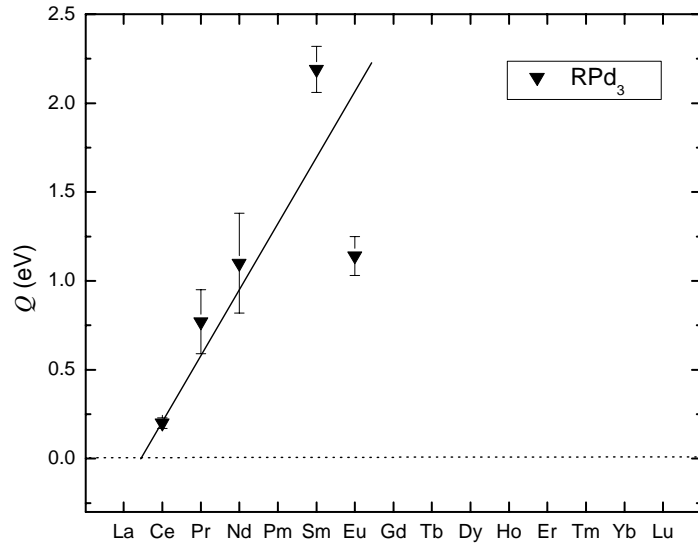
*Fig. A5. Dependence on atomic number of the jump-frequency activation enthalpy
for In/Cd probes in RPd₃ phases.*

Figs. A3 and A5 show linear dependences of both site-preference and jump-frequency activation
enthalpies with atomic number. Fig. A6 shows a plot of jump-frequency activation enthalpies as a
function of lattice parameters. The lattice parameters in Fig. A6 are "out of order" with respect to atomic
numbers because Eu appears to have mixed +2 to +3 valence, giving $EuPd_3$ a larger lattice parameter than
for neighboring lanthanide elements (a graph of lattice parameters vs. atomic number is shown in Fig.
28(b)). As can be seen, the data have a more uniform trend when plotted vs. lattice parameter than when
plotted vs. atomic number.

*Fig. A6. Dependence on lattice parameter of the jump-frequency activation enthalpy
for In/Cd probes in RPd₃ phases.*

A4

5. An overview of jump frequency behavior of Cd-solutes in rare-earth indides, stannides, gallides, aluminides and palladides.

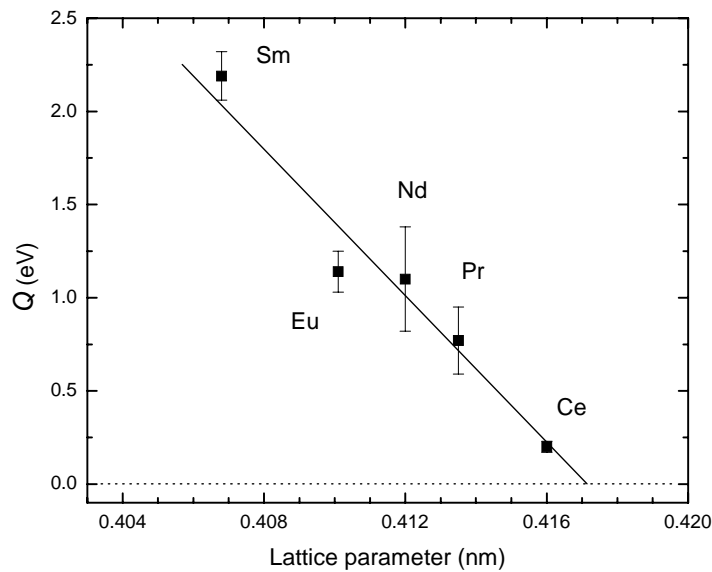Figure A7 gives an overview of jump frequency behavior for In/Cd probes in five families of rare-earth $L1_2$ phases RX_3 that have been studied to date, with X= In, Sn, Ga, Al and Pd. Plotted are inverse temperatures at which jump frequencies reach 10 MHz, T_{10}, versus of lattice parameter. This type of plot was first devised in a study of the indides [3] as a convenient way to summarize behaviors in a large number of phases with a single characteristic quantity T_{10} for each phase. A high value of ordinate $1/k_B T_{10}$ implies a low jump-frequency activation enthalpy.
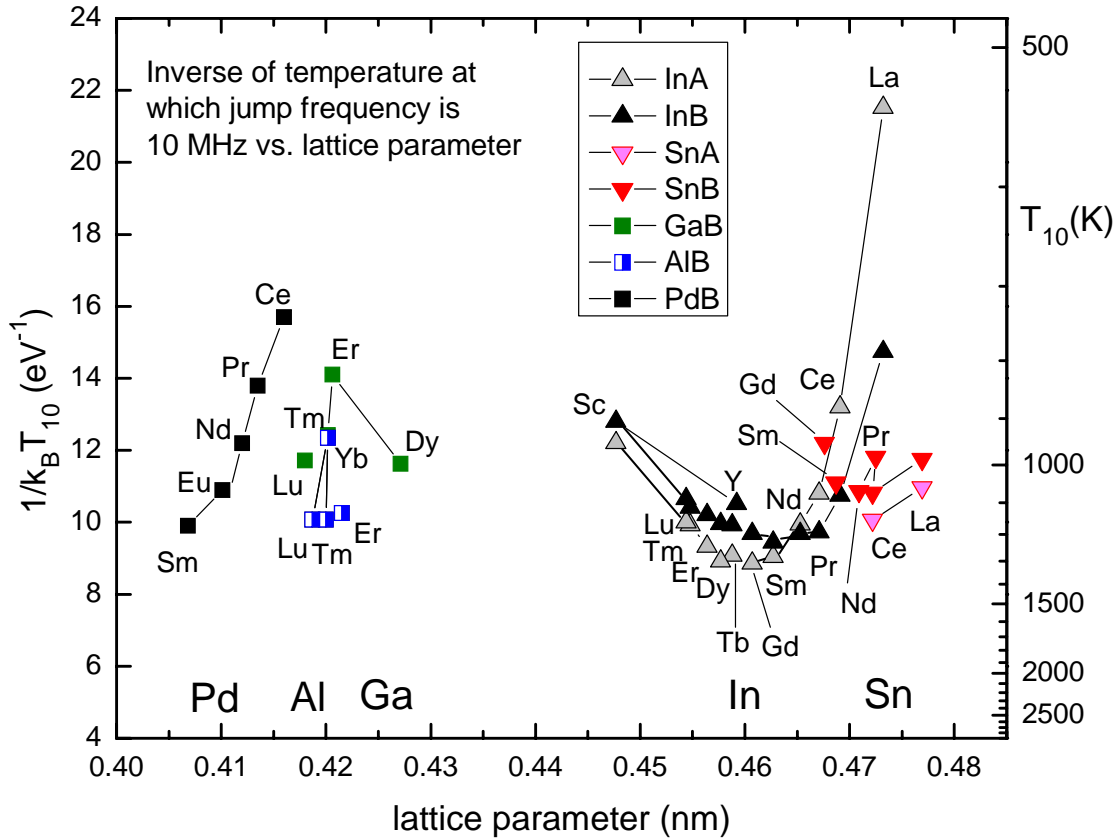
Fig. A7. *Inverse temperatures at which In/Cd solute atoms jumping on the X-sublattice in RX_3 phases are equal to 10 MHz. X-richer and X-poorer boundary compositions are indicated by legends "A" and "B" in the figure.*

Several observations based on Fig. A7 are in order:

- Probes had a strong site preference for X-sites in X-poorer sample. For Pd, Al and Ga phases, almost no probes were detectable on X-sites in X-richer samples. Probes still preferred X-sites in X-richer indides and in $LaSn_3$ and $CeSn_3$. There is no universal dependence on lattice parameter that encompasses all phases.

- The trend to large values of $1/k_B T_{10}$ for lightest and heaviest lanthanide *indides* was attributed to crossover between two diffusion mechanisms in [3]. Note that jump frequencies are greater for In-richer light lanthanide phases and for In-poorer heavy lanthanide phases.

- In series of phases having the same element X, there is "lanthanide contraction" of the lattice parameter along the series attributed to a general decrease in atomic volume of lanthanide atoms. Within individual series, in particular the *indides* and *palladides*, values of $1/k_B T_{10}$ have high values for LaX$_3$ or CeX$_3$ and decrease monotonically along the lanthanide series. This is almost certainly correlated with lanthanide contraction since there is a large volume mismatch between R and X atoms for light lanthanides such as La and Ce that decreases along the series.
- A complete account of trends would need to take into account a large number of factors: volume mismatches of R, X and Cd-probe atoms, effective formation enthalpies of X-vacancies, and enthalpy barriers to jumps of Cd-probe atoms between neighboring sites on the X-sublattices.

6. <u>Search for an underlying correlation between activation enthalpies for jump frequencies and site preferences in the series CePd$_3$ to SmPd$_3$, shown in Figs. A3 and A5.</u>

Both activation enthalpies vary strongly with atomic number. Almost certainly, jumps on the Pd-sublattice are mediated by Pd-vacancies, so that the jump frequency is proportional to the sublattice mole fraction, $[V_{Pd}]$. At the same time, the transfer reaction of probe atoms between R- and Pd-sublattices can be written as $In_R + V_{Pd} \leftrightarrow In_{Pd} + V_R$, so that vacancy concentration $[V_{Pd}]$ enters in analysis of either property. This section outlines thermodynamic models for the two properties under the simplifying assumption of a strictly stoichiometric composition for Pd-poorer samples. Some justification for this assumption comes from values of the Pd-poorer boundary compositions appearing in Table 1, read visually from published binary phase diagrams, that were almost all very close to 75 at.% Pd. While no strong conclusions will be reached, it is thought useful to sketch the general approach.

For the site preference, the thermodynamic model can be based on the transfer reaction $In_R + Pd_{Pd} \leftrightarrow In_{Pd} + Pd_R$ and developed using the law of mass action, leading to equilibrium constant

$$K = \tfrac{[In_{Pd}][Pd_R]}{[In_R]} = \exp(-G_{trans}/k_B T) = \exp\!\left(-(g_{Pd}^{In} - g_R^{In} + g_R^{Pd})/k_B T\right), \tag{A5}$$

in which the brackets identify mole fractions of defects on their respective sublattices and the g's are free energies of formation of the defects. We used $g_{Pd}^{Pd} = 0$ and $[Pd_{Pd}] \cong 1$. The ratio of site fractions for an RPd$_3$ compound is then given by [4]

$$\frac{f_R}{f_{Pd}} = \tfrac{1}{3}\frac{[In_R]}{[In_{Pd}]} = \tfrac{1}{3}[Pd_R]\exp\!\left(+(g_{Pd}^{In} - g_R^{In} + g_R^{Pd})/k_B T\right), \tag{A6}$$

in which [Pd$_R$] is the mole fraction of Pd-antisite atoms on the R-sublattice, either thermally activated or as constitutional defects due to a deviation from stoichiometry,. Note the *positive* sign in the exponential. A way to think of eq. A6 is that if Pd$_R$ were activated with an effective free energy g_R^{Pd}, then $[Pd_R] \approx \exp(-g_R^{Pd}/k_B T)$ and the site-fraction ratio reduces to $f_R/f_{Pd} = 1/3\exp(+(g_{Pd}^{In} - g_R^{In})/k_B T)$. In that case, the activation enthalpy would simply be the difference in site energies of solutes.

Alternatively, starting from the transfer reaction $In_R + V_{Pd} \leftrightarrow In_{Pd} + V_R$ leads to

$$\frac{f_R}{f_{Pd}} = \frac{1}{3}\frac{[In_R]}{[In_{Pd}]} = \frac{1}{3}\frac{[V_R]}{[V_{Pd}]}\exp\left(+(g_{Pd}^{In} - g_R^{In} + g_R^V - g_{Pd}^V)/k_BT\right) \qquad (A7)$$

Thermal activation of point defects can only occur in combinations that preserve the overall composition of the sample. These are enumerated for the $L1_2$ structure in ref. [5], and include formation of an antisite-pair, a Schottky defect combination, and five-defect, etc., defined in eqs. A8 below.

$$0 \to Pd_R + R_{Pd}, \quad K_2 = [A_B][B_A] = \exp(-G_2/k_BT) = \exp(-(g_B^A + g_A^B)/k_BT), \qquad (A8a)$$

$$0 \to 3V_{Pd} + V_R, \quad K_4 = [V_A]^3[V_B] = \exp(-G_4/k_BT) = \exp(-(3g_A^V + g_B^V)/k_BT), \qquad (A8b)$$

$$0 \to 4V_{Pd} + Pd_R, \quad K_5 = [V_A]^4[A_B] = \exp(-G_5/k_BT) = \exp(-(4g_A^V + g_B^A)/k_BT). \qquad (A8c)$$

If all the G's are very high except for one, so that only one defect combination is appreciably activated, then the reactions such as in eqs. A8 become decoupled. For example, if only antisite pairs are thermally activated, then $[A_B] = [B_A]$ and $[A_B] = \exp(-G_2/2k_BT)$ and

$$\frac{f_R}{f_{Pd}} \approx \frac{1}{3}\exp\left(+(g_{Pd}^{In} - g_R^{In})/k_BT\right)\exp(-G_2/2k_BT). \qquad (A9)$$

If only Schottky-defects are thermally activated, then $[V_A] = [V_B]$, $[V_A] = \exp(-G_4/4k_BT)$ and, from eq. A7,

$$\boxed{\frac{f_R}{f_{Pd}} \approx \frac{1}{3}\exp\left(+(g_{Pd}^{In} - g_R^{In} + g_R^V - g_{Pd}^V)/k_BT\right).} \qquad (A10)$$

Five-defects can be formed heuristically by transfer of A-atoms into B-vacancies, in which case $[V_A] = \frac{4}{3}[A_B]$, so that $[V_A] = \frac{3}{4}\exp(-G_5/5k_BT)$.

A more likely scenario is one in which vacancies and antisite atoms form thermally. Let us assume that antisite pairs and five-defects are thermally activated, but that antisite atoms are dominant, so that

$$[A_B] \cong [B_A] \cong \exp(-G_2/2k_BT). \qquad (A11)$$

Inserting eq. A11 into eq. A6 again leads to the very simple expression:

$$f_R/f_{Pd} = 1/3\exp(+(g_{Pd}^{In} - g_R^{In})/k_BT).$$

Jump frequency trends. Trends shown in Fig. A5 or A6 are very systematic. A microscopic model is now developed for an empirical expression for an activated jump frequency: $w = w_0\exp(-Q/k_BT)$. For a vacancy diffusion mechanism, one can express the jump frequency of a diffusing atom as the product of the vibrational frequency of the atom v_0, vacancy mole fraction $[V_{Pd}]$, and probability that the diffusing atom will overcome a migration enthalpy barrier E_{mig} in a jump-attempt:

$$w = \nu_0 [V_{Pd}] \exp(-E_{mig} / k_B T) . \tag{A12}$$

At infinite temperature, the vacancy mole fraction and migration enthalpy factor are both of order 1, so that $w \approx \nu_0$, or about 1 THz. This is consistent with the observed orders of magnitude of the fitted prefactors shown in Table 7. If the composition is strictly stoichiometric, so that there are no structural vacancies, for example, the vacancy concentration will be given by a thermally activated expression:

$$[V_{Pd}] \cong A \exp(-E_{form} / k_B T) , \tag{A13}$$

in which E_{form} is an *effective* vacancy formation enthalpy and $A \approx 1$. Thus, the observed jump-frequency activation enthalpy can be written as the sum $Q \cong E_{form} + E_{mig}$:

$$w = \nu_0 A \exp(-(E_{form} + E_{mig}) / k_B T) \tag{A14}$$

and the trend with lanthanide element may be due to changes in either or both of E_{form} and E_{mig}. For an explicit expression, one can start from eq. A8c (dominant antisite defects + five defects),

$$[V_A] = \frac{K_5^{1/4}}{[A_B]^{1/4}} \approx \frac{K_5^{1/4}}{K_2^{1/8}} = \exp(-(2G_5 - G_2) / 8 k_B T) . \tag{A15}$$

Inserting eq. A15 into eq. A12 leads to

$$w = \nu_0 \exp(-(2G_5 - G_2) / 8 k_B T) \exp(-E_{mig} / k_B T) , \quad w = \nu_0 \exp(-(\frac{G_5}{4} - \frac{G_2}{8} + E_{mig}) / k_B T) , \tag{A16}$$

or, finally, $\qquad \boxed{w = \nu_0 \exp(-(g_{Pd}^V + \frac{g_R^{Pd} - g_{Pd}^R}{8} + E_{mig}) / k_B T)}.$ (A17)

While they are not definitive representations for the site preference and jump frequency, let us consider how eqs. A10 and A17 depend on defect energies. In both cases, the activation enthalpies become *more positive* along the series from CePd$_3$ to SmPd$_3$.

From Fig. A3, the site-fraction enthalpy increases from a large negative value for CePd$_3$ to a small positive value for SmPd$_3$. Possible reasons:

- The site energy difference $g_{Pd}^{In} - g_R^{In}$ is negative, but becomes more positive along the series.
- The vacancy energy difference $g_R^V - g_{Pd}^V$ is negative, but becomes more positive along the series.

From Fig. A5, the jump-frequency activation enthalpy is small for CePd$_3$ and increases rapidly, becoming large for SmPd$_3$ and EuPd$_3$. Possible explanations along the series are that:

- The Pd-vacancy formation energy increases.
- The jump-barrier migration enthalpy increases.
- The antisite-atom energy difference $g_R^{Pd} - g_{Pd}^R$ increases.

A common feature of Eqs. A10 and A17 is that they both contain the factor $\exp\left(-g_{Pd}^{V}/k_{B}T\right)$. This may explain in part the parallel increases in enthalpies with atomic number observed in Figs. A3 and A5, because increases of g_{Pd}^{V} along the series should lead to corresponding decreases in [V_{Pd}].

While both Q's increase with atomic number Z along the series, the rates of increase of the two Q's differ by a factor of two, with dQ/dZ = +0.15 eV for site-preferences (Fig. A3) and +0.36 eV for the jump frequency (Fig. A5).

Although an increase in [V_{Pd}] cannot by itself explain the magnitudes of the changes in Q's, it is satisfying that

1. Matthew O. Zacate and Gary S. Collins, Phys. Rev. B69, 174202 (2004).

2. Egbert R. Nieuwenhuis, Matthew O. Zacate and Gary S. Collins, Diffusion and Defect Data 264, 27-32 (2007).

3. Gary S. Collins, Xia Jiang, John P. Bevington, Farida Selim and Matthew O. Zacate, Phys. Rev. Lett. 102, 155901 (2009).

4. Confer eq. 5 and discussion in the addendum of Matthew O. Zacate and Gary S. Collins, Phys. Rev. B69, 174202 (2004).

5. *Site preference model for hyperfine impurities in compounds*, Gary S. Collins and Matthew O. Zacate, Hyperfine Interactions 136/137, 641-646 (2001).